

October 2020

Convergence of Auditory Nerve Fibers onto Globular Bushy Cells

Matthew Kersting

University of South Florida

Follow this and additional works at: <https://digitalcommons.usf.edu/etd>

 Part of the [Biomedical Engineering and Bioengineering Commons](#)

Scholar Commons Citation

Kersting, Matthew, "Convergence of Auditory Nerve Fibers onto Globular Bushy Cells" (2020). *USF Tampa Graduate Theses and Dissertations*.

<https://digitalcommons.usf.edu/etd/9543>

This Thesis is brought to you for free and open access by the USF Graduate Theses and Dissertations at Digital Commons @ University of South Florida. It has been accepted for inclusion in USF Tampa Graduate Theses and Dissertations by an authorized administrator of Digital Commons @ University of South Florida. For more information, please contact scholarcommons@usf.edu.

Convergence of Auditory Nerve Fibers onto Globular Bushy Cells

by

Matthew Kersting

A thesis submitted in partial fulfillment
of the requirements for the degree of
Master of Science in Biomedical Engineering
Department of Medical Engineering
College of Engineering
University of South Florida

Major Professor: George Spirou, Ph.D.
Paul Manis, Ph.D.
Joseph Walton, Ph.D.

Date of Approval:
October 20, 2020

Keywords: auditory processing, sound localization, three-dimensional modeling, neural circuits,
electron microscopy

Copyright © 2020, Matthew Kersting

Acknowledgments

I would like to express thanks to Carolynna Yamamoto Alves Pinto and Sean Carr for their assistance in segmentation, data analysis, and figure generation, to Robert Nichol and Daniel Heller who provided some much-needed editing to the manuscript, and lastly to all the students who assisted in segmenting the electron microscopy volume.

Table of Contents

List of Figures	iii
Abstract.....	v
Chapter 1: Introduction	1
1.1 The Auditory System	1
1.2 Binaural Hearing	3
1.3 Role of Globular Bushy Cells in Sound Localization	5
1.4 Globular Bushy Cell Physiological Specializations.....	6
1.5 VCN Synaptic Maps	8
1.5.1 Cochlear Root Neurons.....	8
1.5.2 Planar and Radiate Multipolar Cells (Type-1, Type-2 Multipolar; T-Stellate, D-Stellate).....	10
1.5.3 Planar Multipolar	11
1.5.4 Radiate Multipolar	12
1.5.5 Bushy Cells	14
1.5.6 The Role of the Bushy Cell Dendrite	17
1.5.7 Spherical Bushy Cells.....	18
1.5.8 Globular Bushy Cells	19
1.6 Conventional Model for Auditory Nerve Convergence to Globular Bushy Cells	21
1.7 Representing Neuronal Morphology in Silico	22
1.7.1 Segmentation from Image Volume.....	22
1.7.2 Mesh Representation	23
1.7.3 SWC (Skeleton) Representation.....	25
1.8 Modelling Neurons in Silico	26
Chapter 2: Methods	28
2.1 Serial Block-Face Scanning Electron Microscopy.....	28
2.2 Image Segmentation	29
2.3 Extracting and Processing 3D Models.....	29
2.3.1 Converting Segmentations to Meshes.....	29
2.3.2 Mesh Decimation and Smoothing	30
2.3.3 GAMer2 Algorithms	30
2.4 Synapse Quantification	32
2.5 Skeletonization.....	33
2.6 Axon Tracking.....	33
2.7 Computational Modeling.....	34
Chapter 3: Results	35
3.1 Processing 3D Models - GAMer2	35

3.2 Somatic Surface Areas	37
3.3 Apposed Surface Areas	37
3.4 Terminal – Fascicle Relationships	42
3.5 Models of Input Convergence.....	44
3.6 Synapse Distribution	45
3.7 Dendrite Structure	48
Chapter 4: Discussion.....	54
4.1 Precise Meshing Algorithms Allow for More Biologically Realistic Simulations.....	54
4.2 Models of Input Convergence.....	54
4.3 Novel Observations in Electron Microcopy Volume	55
References	58

List of Figures

Figure 1 The synaptic map of the globular bushy cell	20
Figure 2 A neuron cell body represented by a mesh	24
Figure 3 Creating swc files in Syglass	26
Figure 4 The change in surface area during mesh processing	36
Figure 5 Mesh appearance after GAMer2 processing	36
Figure 6 Somatic surface areas of AVCN neurons.....	37
Figure 7 Input ASA for all reconstructed somatic terminals	39
Figure 8 Terminal sizes by axon property	40
Figure 9 The number of convergent auditory nerve terminals to each GBC.....	40
Figure 10 Somatic coverage by large terminals	41
Figure 11 Terminal size distribution	42
Figure 12 Convergence of auditory nerve fascicles to GBCs.....	43
Figure 13 Terminal contribution by fascicle label.....	43
Figure 14 Converging terminals separated by axon property and contacted cell.....	44
Figure 15 Two models of innervation assessed in a computational framework	45
Figure 16 Synapse counts relative to ASA.....	46
Figure 17 Distribution of synapses within the auditory nerve terminal	47
Figure 18 A bushy cell with its dendritic tree and all terminals.....	48
Figure 19 Swellings and shafts on a GBC dendrite.....	50
Figure 20 Distribution of swelling counts per dendrite	50

Figure 21 Composition of GBC dendrite surface area	51
Figure 22 Close-up of the dendritic hub	51
Figure 23 Distribution of hub counts per GBC	52
Figure 24 Unique cytoskeletal structure located in the dendritic hub	52
Figure 25 Distribution of terminals and surface area by dendritic component	53
Figure 26 Large terminals have collaterals branches contacting one another	56
Figure 27 Large terminals have branches that contact neighboring multipolar cells	57

Abstract

Globular bushy cells (GBCs) of the cochlear nucleus are specialized neurons that encode the temporal features of sound. Multiple auditory nerve inputs are known to synapse onto a single GBC, but the exact number and sizes of these inputs have not been systematically investigated in adult mice. To gain a high-resolution and unbiased look at the auditory inputs contacting GBCs, our lab utilized Serial Block-Face Scanning Electron Microscopy. Specifically, 21 GBCs and all their large inputs were reconstructed at nanometer resolution. To produce the most precise results, we applied careful attention to the reconstruction and implemented cutting-edge meshing algorithms.

We found that a range of 5 – 12 large auditory nerve terminals converge onto each GBC, which is higher than previously reported electrophysiological estimates. Interestingly, some GBCs were found to have a single large, dominant input, whereas others did not. Thus, we conclude that there are two models of GBC innervation, i.e., a mixed model (1 or 2 suprathreshold inputs and multiple subthreshold) and a coincidence detection model (all subthreshold inputs). The detailed reconstructions were then combined with a GBC computational model which confirmed the presence of two innervation models. We also present novel discoveries about the structure of GBCs that could only be seen in volume electron microscopy.

Chapter 1: Introduction

1.1 The Auditory System

The mammalian auditory system is a complex pathway consisting of multiple highly interconnected nuclei. It can be functionally and anatomically divided into two general pathways, i.e. the ascending and the descending pathways. The ascending pathway processes and relays information about an organism's environment to the cortex; conversely, the descending pathway relays information from higher-order brain regions, like the auditory cortex, to lower-order brain regions, like the cochlear nucleus (Oliver, Cant, Fay, & Popper, 2018). Our lab mainly focuses on the initial auditory processing center in the brain stem, called the cochlear nucleus, where the peripheral sensory nerve, called the auditory nerve, makes synaptic connections in the CNS.

The auditory system functions to transduce pressure waves in the environment into neural signals. Sound waves cause vibrations in the tympanic membrane, which, in turn, sends pressure waves along the cochlear partition. The vibration of the basilar membrane in response to sound waves causes deflection of the stereocilia of hair cells. Due to the unique structure of the basilar membrane, the audible spectrum of sound frequencies maps smoothly to different locations along the membrane, thereby yielding a frequency to space transformation of the information, called tonotopy. The resulting deflection in the hair cell causes an influx of potassium, leading to membrane depolarization and subsequent neurotransmitter release at synaptic sites on afferent auditory nerve fibers. In the event these afferent neurons generate an

action potential, the neural signal has been initiated and is then sent to processing centers in the brainstem (Purves, Fitzpatrick, & Mooney, 2012).

The cochlea contains a single row of inner hair cells that synapse onto type 1 ANFs. Inner hair cells additionally receive efferent signals from the lateral olivocochlear system to modulate cochlear mechanics. Of special note for this study, multiple type 1 ANFs are innervated by a single hair cell. This arrangement leads to the conclusion that their activity will be highly correlated (Liberman & Oliver, 1984).

Type 1 and 2 ANFs comprise the auditory nerve (AN). The type 1 fibers terminate exclusively in the CN. Upon entry into the CN the auditory nerve fibers bifurcate, sending one branch anteriorly and one branch posteriorly. This bifurcation delineates the two regions of the Ventral Cochlear Nucleus (VCN), i.e., the anterior VCN (AVCN) and posterior VCN (PVCN). Nerve fibers that project posteriorly either terminate at the PVCN or continue through the PVCN to the third subdivision of the CN, the dorsal CN (DCN).

Neural signals that represent auditory information pass through many different nuclei before reaching the cortex and each of these nuclei are specialized to extract certain aspects of sound. This complex afferent pathway is typically oversimplified as a linear system that relays information about the environment to the cortex. However, the actual connections within this pathway are far more complex. Specifically, the nuclei within this pathway are highly interconnected and receive innervation from a variety of other sources. Moreover, ascending projections commonly skip certain nuclei, and the projections are often both ipsilateral and contralateral. This complex system will only be outlined generally here. In short, the axons of the auditory nerve terminate in the Cochlear Nucleus (CN). The CN relays information to the Superior

Olivary Complex (SOC), both ipsilaterally and contralaterally. These bilateral signals are then projected to the Inferior Colliculus (IC), then to the Medial Geniculate Body (MGB), and, finally, to the auditory cortex (Oliver et al., 2018; Purves et al., 2012). Importantly, the tonotopic organization is maintained throughout the multiple nuclei of the auditory pathway.

1.2 Binaural Hearing

The VCN is the first CNS region of the auditory circuit that functions to process sound localization. Two primary output neurons of the VCN are spherical bushy cells (SBCs) and the globular bushy cells (GBCs) (Brawer, Morest, & Kane, 1974; Osen, 1969). Auditory nerve axons form particularly large axo-somatic terminal with SBCs, which are termed endbulbs of Held (Ryugo & Sento, 1991), in the rostral regions of the AVCN. In contrast, GBCs are thought to receive smaller auditory nerve terminals, called modified endbulbs (Rouiller, Capt, Dolivo, & De Ribaupierre, 1986), located in the caudal AVCN, the AN root region, and the PVCN.

Interaural time and level differences are used to locate sound sources along the horizontal plane and these computations are performed in the Superior Olivary Complex (SOC). A precise representation of the temporal features of sound is necessary to perform these computations. Both types of BCs innervate the SOC. Specifically, SBCs project to the ipsilateral Lateral Superior Olive (LSO) and the Medial Superior Olive (MSO) both ipsilaterally and contralaterally, where they form excitatory synapses. Since the MSO receives innervation from both Cochlear Nuclei, it serves as the main CNS nucleus for calculating interaural time differences for lower frequency sounds (Cant & Benson, 2003; Trussell & Oertel, 2018). Alternatively, GBC axonal projections form excitatory synapses with neurons in the ipsilateral Lateral Nucleus of the Trapezoid Body (LNTB), as well as the contralateral Medial Nucleus of the Trapezoid Body (MNTB) where they

form a large terminal, termed the Calyx of Held. Excitatory activity from the VCN drives MNTB inhibition of the ipsilateral LSO (contralateral to the original cochlear nucleus) (von Gersdorff & Borst, 2002). Interaural level differences in higher frequency channels are largely processed in the LSO. This network of inhibitory and excitatory connections ultimately leads to the net excitation of neurons in the LSO located on the side of the body closer to the sound, due to the higher sound intensity (Purves et al., 2012). While the macroscopic neural circuitry of this pathway is well studied, a thorough mapping of individual neuron to neuron connections has not been investigated.

Most of the original studies on bushy cells were conducted in the cat. However, mice are increasingly used as a model organism due to the ability to precisely manipulate genotypes. Therefore, an in-depth analysis of the differences between the species is critically important. Importantly, the low-frequency threshold of hearing is much lower in mice, who hear frequencies only as low as 1-2 kHz, than cats, who can hear as low as 100 Hz (Fay, 1988; Radziwon et al., 2009). Researchers have identified anatomical differences in their auditory pathways that appear to underlie these differences. Specifically, cats have a greater proportion of their tonotopic map associated with low-frequency hearing, the SBC to MSO pathways (Grothe, 2000; Masterton, Thompson, Bechtold, & RoBards, 1975). Fewer large SBCs, with smaller somas and more ambiguous morphologies, have been observed in the mouse (Willard & Ryugo, 1983).

Recent studies show that the differences between the SBC and GBC populations in the mouse are caused more by the synaptic organization than cell morphologies (Lauer, Connelly, Graham, & Ryugo, 2013). This study went on to find several other differences between caudal bushy cells and rostral bushy cells. Caudal bushy cells have fewer, but larger, mitochondria, a

smaller percentage of terminal apposition, a larger percentage of primary terminals, and fewer synaptic vesicles (SVs) around the synapse (Lauer et al., 2013).

1.3 Role of Globular Bushy Cells in Sound Localization

Early physiological studies of the endbulb utilized metal electrodes to record extracellular field potentials of neurons. These studies found a synaptic waveform with three main features. These main features can be attributed to the flow of current into the presynaptic terminal and the cell body. The first component of the waveform is thought to be caused by the incoming action potential, or prepotential, in the presynaptic neuron. The second component derives from the influx of ions through post-synaptic ionotropic transmembrane receptors. The final component of the waveform is driven by action potentials in post-synaptic AVCN cells (Bourk, 1976; Pfeiffer, 1966). The concomitancy of the prepotential and action potential in the postsynaptic neuron is indicative of high synaptic efficacy. In the rostral AVCN, this model has been supported by more modern techniques (Typlt et al., 2010).

The security of this synapse has since been brought into question as a result of the observation of sub-threshold EPSP's in cats (Rhode, 2008; Smith & Rhode, 1987) and prepotentials without a corresponding action potential in gerbils (Englitz, Tolnai, Typlt, Jost, & Rübsamen, 2009; Typlt et al., 2010). Sub-threshold EPSP's indicate that an action potential is not produced every time that the presynaptic cell is active. AVCN bushy cell spike trains that precisely mimic the spike trains of the auditory nerve would implicate a perfectly secure synapse; however, this is not the case (Joris, Carney, Smith, & Yin, 1994). This modulation of the spike train in the AVCN is most likely due to the convergence of multiple auditory nerve inputs (Rothman & Young, 1996; Rothman, Young, & Manis, 1993).

1.4 Globular Bushy Cell Physiological Specializations

Differential activity patterns between the auditory nerve and post-synaptic CN neurons are most often assessed by the construction of peri-stimulus time histograms (PSTHs), which are histograms of neuron spike times given the presentation of a stimulus over many trials. The response differences are binned into a few different types based on the shape of the PSTHs (Blackburn & Sachs, 1989). The GBCs respond with primary-like with notch PSTHs (Bourk, 1976; Rouiller & Ryugo, 1984). Given that ANFs respond with Primary-like PSTHs, the Primary-like with notch PSTHs are similar with the addition of a quick depression in activity after onset and an abrupt firing resumption after the depression in activity. This response pattern encodes the onset of the sound well (Friedland, Pongstaporn, Doucet, & Ryugo, 2003) and is likely caused by the convergence of multiple inputs (Rothman & Young, 1996; Rothman et al., 1993). The Primary-like with notch response patterns have been observed in the caudal regions of the AVCN, where the GBCs are found (Kiang, 1965).

Bushy cells have distinct biophysical properties that enable temporal encoding. For one, these different properties result in very short time-constants (Cao & Oertel, 2010). Specifically, bushy cells have shorter time constants upon depolarization than hyperpolarization. This unique property is mediated by a hyperpolarization-activated conductance and a low voltage-activated potassium conductance. Bushy cells fire transiently when activated and, in response to a hyperpolarizing pulse, undergo strong rectification followed by a hyperpolarizing sag (Cao, Shatadal, & Oertel, 2007). The time course of EPSCs is faster in BCs than the other excitatory cells of the CN (T-Stellate or Octopus cells) (Chanda & Xu-Friedman, 2010). Furthermore, while GBCs are near resting potential, the hyperpolarization-activated conductance keeps the input

resistance of the GBC low. Moreover, the low-voltage gated potassium conductance is activated just above the resting potential. As such, in the event of an EPSP, the potassium conductance is activated and quickly returns to rest, thereby preventing repetitive firing (Cao et al., 2007; Manis & Marx, 1991; Rothman et al., 1993). This conductance determines the precise firing of BCs.

Glutamate is an excitatory neurotransmitter and is released from presynaptic auditory nerve terminals onto bushy cell postsynaptic sites (Hackney, Osen, Ottersen, Storm-Mathisen, & Manjaly, 1996; Jackson, Nemeth, & Parks, 1985; Martin, 1985; Raman & Trussell, 1992; Wang, Wenthold, Ottersen, & Petralia, 1998). At these synaptic sites, NMDARs and AMPARs are localized to the bushy cell postsynaptic membrane. The AMPARs are tetrameric ion channels comprised of a combination of GluR3 and GluR4 subunits (Wang et al., 1998). The presence of these subunits is associated with more rapid gating of the channel (Geiger et al., 1995) and contributes to the temporal precision of the endbulb synapse. Moreover, the postsynaptic membrane of the bushy cell has a higher proportion of AMPARs compared to NMDARs (Rubio et al., 2017) which can influence the velocity of signals. Presynaptic auditory nerve terminals have been shown to dynamically alter neurotransmitter release probability and active zone number to maintain signal fidelity, even during long periods of high sound levels (Ngodup et al., 2015).

Nerve terminals require extensive energy production for vesicular release and calcium buffering. Mitochondria can be anchored to the presynaptic terminal membrane near active zones to ensure metabolic efficiency. The mitochondrion-associated adherens complex (MAC), which functions to tether mitochondria to the pre-synaptic membrane (Spirou, Rowland, & Berrebi, 1998) has been observed in the MNTB (Perkins et al., 2010; Rowland, Irby, & Spirou, 2000), the synaptic target of GBCs. Neuron – neuron connections via gap junctions have also been

observed anatomically between bushy cells, suggesting electrical coupling to enhance synchronization (Ricardo Gómez-Nieto & Rubio, 2009).

1.5 VCN Synaptic Maps

One of the aims of this study is to increase the detail of the bushy cell synaptic map, which we define as a map of the origin, position, and ultrastructural morphology of all synaptic inputs. Here, I will outline the current state of VCN synaptic maps.

1.5.1 Cochlear Root Neurons

There is a group of large neurons inside the AN, but outside of the cochlear nucleus proper, that resemble GBCs (Brawer et al., 1974; De No, 1933; Osen, 1969; Tolbert, Morest, & Yurgelun-Todd, 1982). There are suggestions that these cells are simply displaced GBCs, based on their appearance in Nissl stain, as they commonly have oval somas and eccentrically located nuclei (Webster & Trune, 1982). However, several significant differences have led researchers to conclude that these cells are a unique neuronal subtype, referred to as cochlear root neurons (CRNs).

Several features have been observed that differentiate CRNs from GBCs. First, the somatic diameter differs significantly between root neurons and GBCs. The CRN diameter ranges from 30 – 38 microns; whereas GBCs have diameters that range from 16 – 30 microns (Merchan, Collia, Lopez, & Saldaña, 1988). Interestingly, differences in diameter amongst the bushy cell population have been noted to be based on frequency tuning (Trune & Morgan, 1988). While this could contribute to the somatic diameter difference, the range difference is significant between these cells. The dendritic projections of root neurons are different than those of bushy cells. The root neurons have multiple thick dendrites that are oriented either parallel or perpendicular to the

ANFs (Merchan et al., 1988). However, dendrite trajectories in bushy cells may also be shaped by ANF fascicles and the spatial constraints that they impose (this is a preliminary finding of this study that will not be discussed in detail here), indicating that a distinction based on dendrite orientation may not be meaningful. Furthermore, the CRN soma is not as densely covered by terminals as the GBC (Merchan et al., 1988). The distribution of inhibitory terminals onto the two cells also differs. Glycine and GABA immunolabeling is localized to terminals onto the somatic and primary dendrite regions of GBCs. Conversely, CRNs receive mostly GABAergic terminals that are localized to their dendrites (Kolston, Osen, Hackney, Ottersen, & Storm-Mathisen, 1992).

CRNs can be categorized based on their projection pattern. Whereas GBCs project to the Superior Olivary Complex, particularly the MNTB, CRNs project to a diverse set of brainstem nuclei not restricted to auditory centers. These cells have large axons that project to the Facial Motor Nuclei, Pontine Nuclei, Ventrolateral Tegmental Area, Superior Colliculus, and Periaqueductal Grey. These projections can all be attributed to the role of the CRN in the auditory startle pathway, which mediates an animal's reflex away from a sudden loud stimulus (Horta-Júnior, López, Alvarez-Morujo, & Bittencourt, 2008; Kandler & Herbert, 1991; López, Saldaña, Nodal, Merchán, & Warr, 1999).

CRNs have several auditory nerve synaptic inputs on their soma (Harrison & Warr, 1962; Merchan et al., 1988). These terminals dominate the CRN synaptic map; however, these cells are also innervated by projections from CNS neurons. Specifically, root neurons are postsynaptic partners with neurons in the Ventral Nucleus of the Trapezoid Body (VNTB), as evidenced by anterograde tracing of VNTB axonal projections in the CRNs using electron microscopy. These terminals form symmetric synapses on the soma and dendrite of CRNs (Gómez-Nieto et al.,

2008). The VNTB neurons are likely cholinergic and play a role in auditory prepulse inhibition of the acoustic startle response (Gómez-Nieto et al., 2014). Experiments utilizing anterograde and retrograde tracers have shown evidence for nerve fibers projecting from the Locus Coeruleus (LC) to the CRNs (Gómez-Nieto et al., 2008; Hormigo et al., 2015). In these experiments, LC projections were shown to form small terminals onto the primary dendrite and soma of CRNs. Multiple studies have utilized gene expression and immunohistochemical techniques to suggest that LC to CRN synapses are noradrenergic and serve to modulate the acoustic startle response, depending on the animal's internal state.

1.5.2 Planar and Radiate Multipolar Cells (Type-1, Type-2 Multipolar; T-Stellate, D-Stellate)

A multipolar neuronal subtype was initially identified from Nissl staining based on the shape of the soma (Osen, 1969). Later, these cells were termed stellate due to their appearance in Golgi stain (Brawer et al., 1974). Cant further subcategorized the multipolar neurons of the VCN (outside of octopus cell area) into two groups, type 1 and type 2, based on their appearance in EM (Cant, 1981). This was additionally supported by later studies (Smith & Rhode, 1987). The primary differentiating feature is the lack of somatic innervation in the type 1 cells, although there are also differences in size and endoplasmic reticulum distribution. Later, researchers further delineated two groups of multipolar cells by their projection patterns (Oertel, Wu, Garb, & Dizack, 1990). In short, one group of neurons was found to project axons through the trapezoid body and the other projected dorsally; these neuronal subtypes were termed T-Stellate and D-Stellate, respectively. Finally, two groups of multipolar cells, planar, and radiate multipolar cells, were differentiated using *in vivo* extracellular dye injections (Doucet & Ryugo, 1997; Doucet & Ryugo, 2006). It is now the consensus that planar, type 1, and T-Stellate refer to the same

neuronal subtype, and radiate, type 2, and D-Stellate refer to the same neuronal subtype. Subdivisions have been suggested among these two main subgroups (Doucet & Ryugo, 2006). These subdivisions will not be covered here because there is no known difference in their synaptic map, only their outputs. From henceforth, the two classes will be referred to as planar and radiate multipolar cells.

1.5.3 Planar Multipolar

In contrast to spherical bushy cells, planar multipolar neurons (Type 1) lack a nuclear cap of endoplasmic reticulum. They have very few terminals contacting the somatic surface, instead, the somatic surface is covered by glial cell processes. On their proximal dendrites, small nerve terminals form synapses that have vesicle shapes like those of endbulbs (Cant, 1981). Most terminals that synapse with planar cells contain pleomorphic vesicles; however, terminals with large spherical vesicles (presumably AN) are less frequent. Differences in input profiles have been observed based on characteristic frequency (CF), as terminals with flattened vesicles are more common in the high-frequency region (Josephson & Morest, 1998), but these differences have not been systematically investigated.

Planar multipolar cell activity is typically driven by a few (5 or 6) AN fibers that terminate on the dendrites (Alibardi, 1998; Cant, 1981; Cao & Oertel, 2010; Ferragamo, Golding, & Oertel, 1998). Planar neurons also receive excitatory inputs from other planar neurons and inhibitory endings from radiate neurons (Ferragamo et al., 1998). This input provides broadly tuned inhibition to the planar multipolar neurons (Campagnola & Manis, 2014). The planar neurons also receive inhibition from an unidentified population of neurons in the dorsomedial boundary of the AVCN, where bushy cells are localized (Campagnola & Manis, 2014). They receive glycinergic

inhibition from the vertical cells of the DCN (Wickesberg & Oertel, 1990). This is further corroborated by the presence of glycinergic axonal endings that mainly synapse with primary dendrites (Juiz, Helfert, Bonneau, Wenthold, & Altschuler, 1996).

Some evidence has suggested that serotonin influences planar neurons (Ebert and Ostwald, 1992) and there are serotonergic terminals in the VCN (Klepper and Herbert, 1991; Thompson et al., 1994; Thompson and Thompson, 2001) However, possible serotonergic inputs to planar multipolar neurons have not been conclusively mapped. A similar phenomenon is observed with cholinergic inputs to Planar neurons. In short, cholinergic olivocochlear terminals have been observed in the vicinity of planar cells (Brown et al., 1991; Sherffiff and Henderson, 1994). Moreover, cholinergic VNTB neurons project to the core of the VCN (Fujino and Oertel, 2001). Electrophysiological experiments have shown modulation of planar multipolar neuron activity in response to cholinergic agonists (Oertel and Fujino, 2001). While this evidence is compelling, these synaptic connections have not been mapped at the ultrastructural level. Excitatory planar multipolar neurons (Smith and Rhode, 1989; Zhang and Oertel, 1993; Ferragamo, 1998) predominantly project to higher-order auditory processing regions. However, they also have collaterals that innervate targets within the CN, such as tuberculoventral cells of the DCN (Oertel and Wickesberg, 1993), and have small, round vesicles (Rhode and Smith, 1982).

1.5.4 Radiate Multipolar

In contrast to spherical bushy cells, radiate multipolar neurons (Type 2) lack a nuclear cap of endoplasmic reticulum. Unlike planar multipolar neurons, radiate multipolar neurons have a large degree of somatic terminal coverage (Cant, 1981). Both types of multipolar neurons receive similar types of synaptic inputs; however, the location of those inputs varies.

Radiate multipolar neurons have multiple somatic and proximal dendritic terminal inputs (Smith and Rhode, 1989), and their somas have multiple auditory nerve synaptic inputs (Doucet and Ryugo, 2006). They have collateral branches that project to multiple synaptic targets within the CN, including the DCN, where they stay within their CF range (Spirou et al., 1993), the AVCN, where they synapse with BCs and planar multipolar neurons, and the contralateral CN, where they form synapses with planar multipolar neurons (Rhode and Smith, 1985; Ferragamo et al., 1998; Smith, Massie, Joris 2005; Needham and Paolini, 2006; Oertel et al., 2011). These axon collaterals have terminals with pleomorphic vesicles (Rhode and Smith, 1986; Smith, Massie, Joris, 2005), thereby corroborating their inhibitory nature.

Campagnola and Manis (Campagnola & Manis, 2014) used several different techniques to study how the radiate multipolar neurons influence other cells in the VCN. They found that these cells provide spatially broad inhibition of planar multipolar neurons and bushy cells. The inhibition provided to planar multipolar neurons spans twice the frequency range as that provided to bushy cells.

Radiate multipolar neurons use glycine as their neurotransmitter (Wenthold, 1987; Alibardi, 1998; Doucet et al., 1999; Doucet and Ryugo, 2006). Subdivisions of the radiate multipolar neuron class have been suggested based on their projection patterns (Doucet and Ryugo, 2008). Some radiate neuron axons project to the contralateral CN, where they form symmetric synapses with pleomorphic vesicles and have even been shown to contact a bushy cell (Brown et al., 2014).

1.5.5 Bushy Cells

Bushy cells are the most well-studied cell type in the CN. Initially termed brush cells based on the Golgi stained appearance of their dendrites (Lorente de No 1934), they were renamed bushy cells, also based on labeling of their dendrites by Golgi stain (Brawer, Morest, & Kane, 1974) and more modern neural tract tracing molecules. Using Nissl stains, Bushy cells were later subdivided into spherical and globular subtypes according to somatic morphology and the central (spherical) or eccentric (globular) location of the nucleus. This distinction was initially identified in the cat cochlear nucleus and further correlated with Golgi and EM studies in the same species. SBCs were found to be localized to the rostral AVCN, and GBCs posteriorly in the AVCN and extending into the PVCN (Osen, 1969; Cant and Morest, 1979; Tolbert, Morest, and Yurgulen-Todd, 1982).

The dominant synaptic inputs to bushy cells are large terminals of auditory nerve fibers called endbulbs of Held (Ramon y Cajal, 1909; Brawer and Morest, 1975; Roullier et al., 1986). The larger endbulbs are present in the anterior AVCN and smaller endbulbs, called modified endbulbs are found more caudally, localized to the spherical and globular cell regions, respectively (De No, 1933; Manis, Xie, Wang, Marrs, & Spirou, 2012; Rouiller, Cronin-Schreiber, Fekete, & Ryugo, 1986; Rouiller & Ryugo, 1984). Note that both spherical and globular cell distributions are innervated by auditory nerve fibers that span the audible spectrum, with high frequencies represented dorsally and low frequencies ventrally (Muniak et al., 2013), so each BC has a characteristic frequency (CF).

The distinction of bushy cell subpopulations is less clear in rodents, where there may be a continuum of morphological features (Willard and Ryugo, 1983; Trettel and Morest, 2001;

McGinley and Oertel, 2006; Cao and Oertel, 2007). Nonetheless, some distinctions have been observed in rodent models. Electrophysiological and structural differences in the rostral-caudal innervation of bushy cells have been measured, whereby fewer endbulbs contact bushy cells in the rostral AVCN (Lauer et al., 2013; Cao and Oertel, 2010). However, a more in-depth, systematic investigation of large numbers of cells, mapped to their spatial locations, is necessary to clarify this topic.

Detailed anatomical studies suggest that the bushy cells receive various somatic and dendritic (particularly primary dendrite) synaptic inputs from multiple sources (Spirou et al., 2005; Gomez-Nieto and Rubio, 2009). This observation is supported by earlier electron microscopy studies that described a variety of terminal types on bushy cells. The dominant input is a terminal containing spherical vesicles and multiple asymmetric synapses. Importantly, these terminals degenerate after cochlear ablation, leading to the conclusion that they are ANF terminals (Cant and Morest, 1979; Tolbert, Morest, and Yurgelun-Todd, 1982). Furthermore, the main AN synaptic input with bushy cells is somatic (endbulbs and modified endbulbs), but there is evidence that bushy cells also receive smaller AN inputs localized to their dendrites. The primary targets of inhibitory inputs onto bushy cells are the soma and proximal dendrite (Gomez-Nieto and Rubio 2009; Gomez-Nieto and Rubio, 2011).

Type 1 ANFs are classified by their rate of spontaneous discharge (Liberman, 1991). However, the precise details of bushy cell innervation by these groups has not been comprehensively studied. Studies by Ryugo and colleagues have assessed the anatomical differences in endbulb terminals of different AN fiber groups. They found that AN fibers with high rates of spontaneous discharge typically have endbulbs with numerous, but small, synaptic

specializations (Ryugo et al., 1996). They also found that endbulbs from deaf cats have larger synapses (Ryugo et al., 1997). These data suggest that AN fiber activity increases the number of synaptic specializations but decreases their size. These results have been further strengthened considering a more recent study that showed a possible linear relationship between synapse size and strength (Holler-Rickauer et al., 2019). Moreover, recent evidence suggests that the endbulbs synapse utilizes both chemical transmission, via glutamate, and electrical transmission, via gap junctions (Rubio and Nagy, 2015). Bushy cells also may receive some innervation from type 2 ANFs, although how frequently this occurs is unclear. These smaller terminals synapse with the soma and primary dendrites of bushy cells, although the main target of these fibers is the granule cell domain (Benson and Brown, 2004).

To further understand the nature of different synaptic bushy cell dendritic inputs, researchers have characterized different nerve terminal types using various presynaptic markers. Specifically, VGlut1, VGlut2, and VGAT have been localized to the bushy cell dendritic compartment (Gomez-Nieto and Rubio, 2009). VGlut1 labels small auditory nerve terminals on bushy cell dendrites that drive the smaller excitatory peaks observed in the BCs when innervating the AN (Young and Sachs, 2008). VGlut2 labels non-AN glutamatergic inputs, possibly originating from somatosensory brainstem nuclei (Sp5) (Li and Mizuno, 1997; Heeringa et al., 2018). While this data showing innervation from somatosensory nuclei is intriguing, high-resolution visualization of Sp5 nerve terminals on bushy cells has not been shown. Moreover, the physiological effects of Sp5 stimulation on bushy cell activity could be explained by secondary inputs from other VCN cells. Finally, VGAT is a marker for GABAergic synapses. Two possible sources of VGAT localization to presynaptic terminals that appose bushy cell dendrites have been

proposed. First, VCN local circuitry utilizes neurons with mixed glycinergic and GABAergic synapses (Kolsten, et al., 1992). Second, there are also descending inputs from the SOC that use both transmitters (Ostapoff et al., 1997).

While BCs do not have axon collaterals within the CN, there is evidence of gap junctions between BCs. Studies by Rubio and colleagues have provided more convincing results. Specifically, in rats and monkeys, cell bodies and primary dendrites stain positively for connexin proteins (which facilitate gap junction communication) (Gomez-Nieto and Rubio, 2009; Rubio and Nagy, 2015), suggesting an electrical coupling between bushy cells. Conversely, an experiment using biocytin, a gap junction permeable tracer, found no spreading of the dye between bushy cells (Cao et al., 2007). However, since this biocytin tracing technique is imperfect (see Rubio and Nagy, 2015), no consensus has been reached.

Bushy cells are inhibited by D-Stellate neurons (Campaglona and Manis, 2014), which are tuned to a broad frequency range (Palmer et al., 1996; Smith and Rhode, 1989) and likely form glycinergic synaptic inputs with BCs (Doucet and Ryugo, 2006). These synaptic inputs are likely contributing to the sideband inhibitory properties observed in SBCs (Caspary, Backoff, Finlayson, & Palombi, 1994; Goldberg & Brownell, 1973; Keine, Rübtsamen, & Englitz, 2017; Spirou, Brownell, & Zidanic, 1990). Bushy cells also receive sharply tuned inhibitory signals from the vertical cells of the DCN and an unidentified cell population in the dorsomedial boundary of the AVCN (Campaglona and Manis, 2014).

1.5.6 The Role of the Bushy Cell Dendrite

The BC dendritic tree has one or two primary dendrites, which in turn branch extensively over a short distance, creating a “bush” like appearance, and the distal dendrites often appear

beaded (Cant and Morest, 1979a; Tolbert et al., 1982; Rouiller and Ryugo, 1984). The functional role of this unique dendritic tree is not well understood. A recent study analyzing the role of MNTB principal cell dendritic processes found a positive correlation between dendrite size and the time constant of the neuron (Von Gersdorff 2019). This result is especially interesting considering that GBCs innervate the MNTB principal cells and, like MNTB principal cells, GBCs are known for receiving large somatic inputs. BC dendritic arborizations often branch around other BCs forming BC clusters, suggesting some coupling of their activity (Ricardo Gómez-Nieto & Rubio, 2009).

Three types of immunofluorescent markers are observed on the bushy cell dendrites (VGLUT1, VGULT2, VGAT). VGLUT1 primarily labels auditory nerve terminals and VGLUT2 primarily labels non-auditory inputs (Nakamura et al., 2005; Zhou et al., 2007). The primary dendrite receives a higher percentage of inhibitory terminals while the distal dendrites receive a higher percentage of excitatory terminals. The auditory nerve terminal occasionally forms divergent contacts, where a large terminal on the soma will also form synapses on passing BC dendrites (Ricardo Gómez-Nieto & Rubio, 2009).

1.5.7 Spherical Bushy Cells

Different types of synaptic terminals are seen covering the soma, proximal dendrite, and axon hillock of SBCs. The largest innervating terminal on an SBC contains large, spherical synaptic vesicles and can be degenerated by cochlear ablation, which has led to the conclusion that these terminals are endbulbs (Cant and Morest, 1979). Additionally, some data indicate that the large endbulb contacting SBCs occurs preferentially through the high spontaneous rate AN fibers

(Spirou et al., 1990). There are clusters of GABAergic and Glycinergic terminals, glycinergic being more common (Moore and Moore, 1987; Juiz et al., 1996).

To study the architecture of the endbulb at high resolution, researchers have visualized SBCs using serial-section electron microscopy (ssEM). While this article exclusively refers to the cells as bushy cells, we infer that they are SBCs, considering the image volume was taken from the rostral half of the AVCN. The authors reconstructed seven endbulbs in the rostral half of the AVCN that contained an average of 155 synaptic specializations. On one particular SBC, reconstructions showed the presence of 4 large AN inputs. Importantly, this input number is higher than the number proposed by electrophysiological studies (Cao and Oertel, 2010). The 4 endbulbs contacting the cell were well separated and often covered by glia, which can help isolate individual endbulbs activity. The number and sizes of converging AN terminals differ considerably from what has been observed with GBCs in the AN root region (Nicol and Walmsley, 2002).

1.5.8 Globular Bushy Cells

GBC cell bodies are extensively innervated by multiple types of synaptic terminals. The modified endbulb terminal dominates these somatic inputs (Liberman, 1991) and, collectively, terminals cover approximately 85% of the cell surface (Spirou, Rager, & Manis, 2005). These terminals also synapse on the primary dendrite and the axon hillock (Tolbert and Morest, 1982; Ostapoff and Morest, 1984). While the modified endbulbs that synapse with GBCs are generally smaller than those onto SBCs, GBCs do receive some larger synaptic inputs (Rouiller, Cronin-Schreiber, et al., 1986) and these size of these modified endbulbs is still considerably larger than a typical nerve terminal.

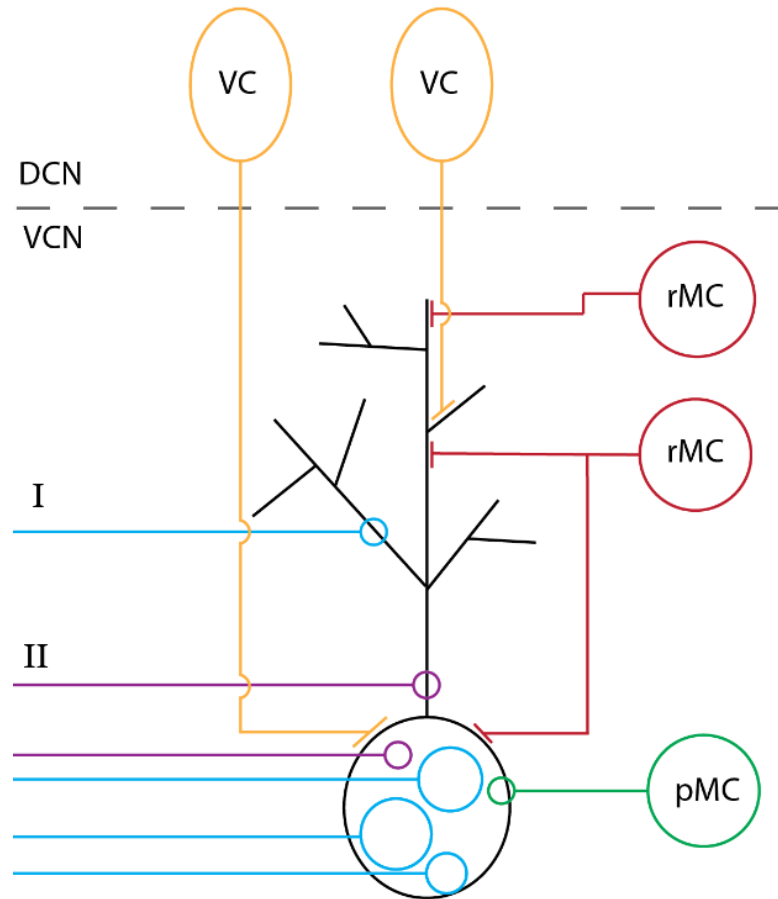


Figure 1 The synaptic map of the globular bushy cell

Presynaptic terminals with pleomorphic or small round vesicles more commonly localize to the more distal dendrites of GBCs (Ostapoff & Morest, 1991). Moreover, the various types of synaptic terminals densely distribute on the soma, primary dendrite, and even the axon initial segment (Smith & Rhode, 1987; Tolbert et al., 1982). Conversely, the distal dendrites are sparsely innervated and receive terminal contacts containing flat and pleomorphic vesicles (Smith & Rhode, 1987). The density of presynaptic terminals is inversely correlated with the distance from the soma, except for terminals presumed to be GABAergic, which innervate the dendritic processes at a constant density (Ostapoff & Morest, 1991). These data are corroborated by the

finding that GBCs are innervated by glycinergic and GABAergic terminals that localize predominately to somatic and primary dendritic compartments (Kolston et al., 1992).

The average number of AN input convergence onto GBCs was initially estimated to be around 20 per GBC in the cat (Liberman, 1991; Spirou et al., 1990). More recently, ssEM has been used to more accurately visualize and quantify the number of AN inputs. Previous data from our lab show that GBCs receive a wide range of AN inputs, between 9 and 69, with an average of 15 to 23 inputs (G. Spirou et al., 2005). In mice, the rates of convergence were examined using electrophysiological measurements (Cao & Oertel, 2010) and found to be far lower (4 or 5) than in cats. However, electrophysiological measurements of convergence are prone to underestimation.

1.6 Conventional Model for Auditory Nerve Convergence to Globular Bushy Cells

The average number of auditory nerve inputs onto the excitatory neurons of the AVCN was previously quantified in the Oertel laboratory; Spherical bushy cells- 2, globular bushy cells- 5, and T-Stellate- 6.5 (Cao & Oertel, 2010). These rates of convergence were quantified via stimulation of the presynaptic AN root with increasing voltages to recruit additional inputs and measurement of the number of steps in the Excitatory Post-Synaptic Potential (EPSP) of the postsynaptic cell. This process is prone to underestimation for a few reasons: 1 – axons may be cut as this is a slice preparation experiment 2- multiple axons can be recruited simultaneously 3- small inputs may be unresolved. Since convergence rates will influence the processing of auditory signals, this ambiguity warrants further investigation. One of the main goals of this thesis will be to quantify the number of converging auditory nerve terminals onto the GBCs in the mouse using an unbiased and high-resolution approach to counting terminals.

1.7 Representing Neuronal Morphology in Silico

1.7.1 Segmentation from Image Volume

The raw data for this study is in the form of a 3-dimensional image volume or a 3-dimensional matrix of grey-scale values. It is important, at least in this case, to have some meta-data in the file that can bring us from pixel-dimensions to physical dimensions. For instance, in this study, each voxel is 5.5 nm in x and y dimensions and 60 nm in the z dimension. Issues with the anisotropic nature of this volume will be discussed later. The amount of physical distance between two voxels gives us all the information needed to extract features such as surface area and volume.

The original volume can be noisy, so a process of “binning” is often used. Calling the original volume bin one we move to bin two by averaging four neighboring voxels in the x-y plane and making that the matrix value for the new volume. This increases the signal-to-noise ratio and makes the file 1/4th the original size. The voxel dimensions double in the x-y plane. Due to the anisotropic nature of the volume binning is not done in the z-dimension, with anisotropy in the z-dimension stemming from the slice thickness of the tissue during imaging.

For segmentation, label image volumes need to be created for each object of interest. The biggest difference between a label file and the original image file is that each position in the matrix of the label file can be represented by two states, as the object of interest is either in that location or not. Several programs can be used to create these segmented files, all of which accomplish the same task, load an image volume, and allow the user to select which voxels are part of the segmented volume. Several image processing techniques can do this automatically, but the application of these to EM data is still in the works. The simplest is a flood-filling algorithm

and the most complex are modern-day machine-learning algorithms (Januszewski et al., 2018; K. Lee et al., 2019). Due to the high complexity of the structures in our study and the desire for extreme accuracy, we implemented the manual segmentation method. This is where a trained person will sit down with the image volume and segment a structure of interest.

To save file space the segmented structures do not encompass the entire image volume. To know how the segmented file and the original image volume align, some additional information is stored in the segmented file. For the original volume, we need to keep track of the voxel dimensions, for the segmented volume we need to keep track of the dimensions as well as the origin. This allows us to translate the segmented volume to its position in the image volume.

1.7.2 Mesh Representation

To visualize the segmented structures, we use a mesh representation. The meshes used here are face-vertex meshes. These files are a series of vertices, each representing a point in 3-D space, and a series of triangular faces, indicating which vertices are connected. A normal vector can also be attributed to each face, or each vertex (being an average of the normals of the connecting faces). The mesh representation allows us to create geometrically precise models that can be visualized in 3D space. This also allows us to use popular rendering platforms such as Blender (Blender Foundation - <http://www.blender.org>) for visualizations.

The meshes in this study were reconstructed by segmenting at high-resolution (11 x 11 x 60 nm). An algorithm called “marching cubes” is used to create each mesh (Lorensen & Cline, 1987). This process looks at 8 locations in the segmented image volume at a time, in the shape of a cube, and places vertices and faces depending on which locations contain the object and which do not. After running this algorithm on segmented volumes at high-resolution meshes

containing 1 million or more vertices are generated, which lead to inaccuracies in quantification. Furthermore, meshes of this size lead to slow processing and rendering times for visualization and quantification, so the meshes must be decimated (reduction in the total number of vertices). The most common method of mesh decimation is vertex clustering, whereby neighboring vertices are merged into one another and the faces around them are rearranged (Low & Tan, 1997). Smoothing is also performed on the meshes because anisotropic voxels lead to a “stair-step” effect on the meshes. In Blender, smoothing is performed by moving each vertex towards the average location of all its neighboring vertices. The amount the vertex is moved can be modified by the user with a strength value.



Figure 2 A neuron cell body represented by a mesh

Some issues arise when using Face-Vertex meshes with such complicated objects, especially when the goal is to preserve as much of the geometry as possible. After processing the

mesh there are often intersecting faces or non-manifold edges. An intersecting face is defined as two faces of the mesh passing through one another. A non-manifold edge is an edge that is not connected to 2, and only 2, faces. Both issues are biological impossibilities and must be resolved. Non-manifold edges and intersecting faces can be resolved by either selecting the problematic vertices and “dissolving” them whereby the vertex is deleted, and the geometry is healed or by fixing the issue manually whereby the vertices are positioned by the user.

1.7.3 SWC (Skeleton) Representation

The SWC representation is the simplest and most lightweight. The swc file contains a series of connected nodes, each with an x,y,z coordinate, a radius, and a parent node. This file is typically created manually, although there are efforts to automate the process (<https://github.com/seung-lab/kimimaro>). To create an swc file, one can either look at the raw image volume, a segmented volume, or a mesh file. To start the file an origin node is placed, and it is assigned a radius. From here each successive node is placed and the parent is inferred as the node placed previously. To create a branch, a non-terminal node is selected, and the branch runs from there. The swc file can be as detailed as the user desires. These files are often created from confocal or 2-photon microscopy images, with these imaging methodologies leading to lower resolution swc files compared to the methods that we utilized creating them from an already segmented electron microscopy volume. The swc file is important for our usage because they can be easily converted to hoc files that are used in the NEURON simulation environment (Carnevale & Hines, 2006). To help process these models a custom-written python package was developed in the lab (<https://github.com/MCKersting12/pyswc>). This python package allows for processing

operations such as scaling and rotating. Other software was also developed in the lab to analyze swc files and they are typically built on top of this package.



Figure 3 Creating swc files in syGlass

1.8 Modelling Neurons in Silico

The study of Cao and Oertel 2010 found that the bushy cells in the auditory nerve root region have an average number of 5 auditory nerve inputs. However, their methodology is susceptible to underestimation. A more definitive understanding of the number of auditory nerve inputs onto GBCs and their relative sizes is important for the construction of biologically realistic computer simulations. This study will also highlight other aspects of GBC morphology that have not been systematically investigated. This information is incorporated into a computational model of the GBC created by our collaborator Dr. Paul Manis at UNC-Chapel Hill (Paul B Manis & Campagnola, 2018). This model is a python-based interface to the NEURON simulator. It is a general-purpose model of the cochlear nucleus but also supports detailed neuron

representations. Some results from the modeling will be shared here, but they will not be covered extensively.

Chapter 2: Methods

2.1 Serial Block-Face Scanning Electron Microscopy

Following transcardial perfusion, tissue was sectioned at 200 μm thickness from the caudal regions of the AVCN, in the auditory nerve root, of an adult (P60) FVB/NJ mouse (NCI; Frederick, MD and Jackson Laboratory; Bar Harbor, ME). This region was selected because it is dominated by GBCs (Nell B. Cant & Morest, 1979; Osen, 1969; Tolbert et al., 1982). The tissue sections were prepared for Serial Block-Face Scanning Electron Microscopy Imaging (SBEM) using the protocol outlined in Deerinck, Bushong, Thor, & Ellisman, 2010. One section was trimmed and mounted for imaging sectioning. A volume of $148\mu\text{m} \times 111\mu\text{m} \times 158\mu\text{m}$ was imaged with a pixel dimension of 5.5 nm and slices were cut at a thickness of 60 nm. Imaging was performed using a pixel dwell time of 0.5 μs , and the imaging run required 7.5 days. The image volume contained 31 complete Cell bodies, including 27 GBCs. GBCs were differentiated from multipolar cells by the presence of only 1 or 2 dendrites, roughly globular somas, and the presence of large auditory nerve terminals.

Due to the large size of the volume (1.6 TB) and the goal of reducing noise in the image, most of the analysis was performed by downsampling in the image plane. Voxel averaging at 2 x 2 binning increased the dimensions of each voxel to 11.0nm x 11.0 nm x 60.0nm. With these imaging parameters, synaptic vesicles can be visualized as well as a post-synaptic density which appears as darkening on the post-synaptic membrane. Large axons of the auditory nerve, dendrite processes, and globular bushy axons can be identified and accurately reconstructed.

2.2 Image Segmentation

Seg3D (University of Utah, Scientific Computing and Imaging Institute) was used to segment the structures of interest from the raw data volume. A Seg3D volume was created from the tiff stack by using the “Create Large Volume” tool supplied by the program. This tool creates a version of the image volume that can quickly load different resolutions while using the program. When the user is zoomed out, a lower resolution block will be rendered to increase processing speed to allow for interactive use of the entire ~250 GB volume. In Seg3d you can create segmentation masks by cropping a region of interest and adding a new mask to that layer. On the masks, the paintbrush tool is used to carefully trace the region of interest.

Structures of interest were identified and segmented according to accepted morphological criteria (Peters, Palay, & Webster, 1992). Somata contained nuclei and prevalent Golgi and endoplasmic reticulum. Dendrites and axons were identified by looking for processes extending from the soma and following them through the volume to their termination. Dendrites branched frequently and were sites of neural input, axons typically became myelinated within the volume. Nerve terminals were identified by the presence of synaptic vesicles and a post-synaptic density on the apposed cell. Afferent axons were tracked from their terminal to the edge of the volume.

2.3 Extracting and Processing 3D Models

2.3.1 Converting Segmentations to Meshes

In Seg3D, 3D models of the structure of interest are created by running the “create isosurface” command. This performs the marching cubes algorithm that takes in volumetric image data and returns a mesh file. This mesh file is saved as a vtk file. The vtk format is not

widely used, so a custom python script was written to convert this file into the more commonly used obj format. From here the mesh file can be imported into 3D modeling software for processing and analysis.

2.3.2 Mesh Decimation and Smoothing

The meshes in .obj format are loaded into Blender for processing. The meshes created are unnecessarily detailed which leads to large file sizes. To fix this the meshes are decimated, typically until they consist of around 100,000 vertices. This is performed in Blender by using the decimate modifier in collapse mode. This merges neighboring vertices progressively while considering the shape of the mesh (Low & Tan, 1997). The meshes are then smoothed for appearances using the smooth modifier. This modifier smooths the mesh by flattening the angles between adjacent faces in the mesh. This modifier provides a factor and the option of a repeat number. These can be manipulated by the user to end with a smooth mesh that has not lost much of its geometry. While these mesh processing steps are suitable for visualization, we found that taking metrics like surface area or volume leaves large room for error. Because of these issues, we evaluated more consistent mesh processing algorithms.

2.3.3 GAMer2 Algorithms

We implemented a more advanced and accurate mesh by applying the GAMer2 algorithms and procedures (C. Lee et al., 2020). The results of these steps will be discussed in the results section, and in this section, the algorithms behind GAMer2 will be outlined. GAMer2 was created to create adequate methods for Finite Element Analyses bound by meshes, and we and others found that it also reduces the error for metrics like surface area and volume (Kerr et al., 2008).

In GAMer2 a local structure tensor (LST) is constructed for each vertex (Fernández & Li, 2003; Haußecker & Jähne, 1996; Knutsson, 1989). The tensor for a vertex – v is constructed by analyzing the normal vectors of the vertices in the local r – ring neighborhood. Each normal vector is broken down by its x , y , and z components and summed as outlined in the formula.

$$T(v) = \sum_{i=1}^{N_r} n_i \otimes n_i = \sum_{i=1}^{N_r} \begin{pmatrix} n_i^x n_i^x & n_i^x n_i^y & n_i^x n_i^z \\ n_i^y n_i^x & n_i^y n_i^y & n_i^y n_i^z \\ n_i^z n_i^x & n_i^z n_i^y & n_i^z n_i^z \end{pmatrix}$$

The eigendecomposition of the LST finds the dominant orientations of the normal vectors in the neighborhood around the vertex of interest (Weickert, 1998). By using the LST to weight the movement of vertices during smoothing algorithms, the geometry of the object can be retained while smoothing the mesh.

Two smoothing algorithms were implemented in the current study – the angle-weighted smoothing (Zhou & Shimada, 2000) and the normal smoothing. Angle-weighted smoothing is performed by analyzing the immediate neighbors of a vertex of interest. Two adjoining line segments are analyzed at a time, a plane that bifurcates the angle between these segments is created and the vertex of interest is projected onto this plane. This is repeated for each pair of adjoining line segments and the vertex is moved towards the average position. In the following equations, α is inversely proportional to the angle between the vertices, \dot{x} is the new target location, \hat{x} is the new location after weighting, λ is an eigenvalue, E is an eigenvector and e represents the edge vector that spans between two vertices.

$$\alpha_i = \frac{e_{i-1} * e_{i+1}}{|e_{i-1}| * |e_{i+1}|}$$

$$\dot{x} = \frac{1}{\sum_{i=1}^n (\alpha_i + 1)} \sum_{i=1}^n (\alpha_i + 1) x_i$$

The vertex is not moved directly to the newly calculated position, as its movement is weighted by the LST. This LST weighting serves to lessen the movement of the vertex in directions of high curvature. This algorithm also has the benefit of moving the median triangle angle closer to 60 degrees, a characteristic of a well-conditioned mesh (Shewchuk, 2002).

$$\hat{x} = x + \sum_{k=1}^3 \frac{1}{1 + \lambda_k} [(\dot{x} - x) * E_k] E_k$$

The normal-based smoothing algorithm (Chen & Cheng, 2005; Yu & Bajaj, 2004) is used to further smooth the mesh. This moves a vertex of interest by analyzing the local face normal vectors. Analyzing the vertex x each connected face is analyzed. The face n_i has three neighboring faces, the average of those three normal vectors is computed and the vertex is rotated around edge e such that its normal vector n_i becomes equal to the calculated average. This is performed for all the faces around x and the vertex is moved to the average of these projections. In this equation \hat{n}_i is the new normal vector n_{ij} represents a neighbor normal vector, and K is a user defined parameter.

$$\hat{n}_i = \frac{1}{\sum_{i=1}^3 e^{K(n_i * n_{ij})}} \sum_{i=1}^3 e^{K(n_i * n_{ij})} n_{ij}$$

2.4 Synapse Quantification

Each input contains multiple synapses, so the number of synapses was quantified for 23 terminals of varying sizes. This was done to assess the number of synapses per μm^2 of contact area. Synapses can be identified in EM by clustering of synaptic vesicles in the pre-synaptic cell, a slight concavity in the post-synaptic membrane, and a post-synaptic density (Peters et al.,

1992). The number of synapses per μm^2 was averaged and this average was used to estimate the number of synapses in each terminal based on its contact area.

2.5 Skeletonization

Skeletonizations were performed in syGlass (IstoVisio, Inc.). Volume information was also preserved in these files by including a radius at each node. Meshes were imported and the skeletons were created by using the “tracing” tool. Since these skeletons were created from a mesh that was reconstructed at nanometer resolution, they are the most accurate in the literature. Special node types were created to highlight the features of GBCs. The swc file is important for our usage because they can be easily converted to hoc files that are used in the NEURON simulation environment. To help process these models a custom-written python package was developed in the lab (<https://github.com/MCKersting12/pyswc>).

2.6 Axon Tracking

Terminal axons can be tracked throughout the volume, so the morphological properties were noted. Large groups of axons (fascicles) traverse the volume cohesively. In the rostral-caudal planes, these fascicles constitute auditory nerve fascicles. Branches from axons within the fascicles that led to endbulb terminals were tabulated. The axon properties were divided into 3 categories: 1- Myelinated and From Fascicle; 2- Myelinated and Not from Fascicle; 3- Unmyelinated. This property was assessed for all large terminals onto GBCs. To visualize the connection to fascicles, 2 cells were selected, and their entire axon was segmented using the tracing tool in syGlass.

The number of axons in all fascicles was also quantified to determine whether some fascicles preferentially target the cells in our volume. Major fascicle labels were created for

fascicles that never merge, minor fascicle labels were created for groups of axons that are merged over some distance and separate from one another within the volume. Each of the axons tracked from large terminals into a fascicle was assigned to one of these labels.

2.7 Computational Modeling

The quantification of terminal count, terminal size-distribution, and cell surface area was incorporated into a detailed computational model of GBCs so that the response properties can be assessed. Details on how the Manis Lab has created the model of the AVCN can be found at Manis, P.B., Campagnola, L., A biophysical modelling platform of the cochlear nucleus and other auditory circuits: From channels to networks, *Hearing Research* (2018), <https://doi.org/10.1016/j.heares.2017.12.017>. This model has considered the main results of physiological studies in the AVCN and will be used here to assess the convergence rates of auditory nerve inputs onto GBCs. All electrophysiological results included in this study are from experiments done within the model.

Chapter 3: Results

3.1 Processing 3D Models - GAMer2

Based on recommended procedures from Lee et al., 2020, and experimentation described here, all meshes were processed in the same manner. An initial vertex decimation was performed, made necessary by the size of meshes generated by performing marching cubes on an image volume reconstructed at such high-resolution and anisotropic sampling during imaging. Meshes typically contained greater than 1 million vertices before decimation, which leads to very large times to perform smoothing algorithms and rendering. Depending on the object of interest, decimation was designed to generate meshes containing 100,000 – 300,000 vertices, at this point we found very little change in the geometry and processing times were more manageable. Experimentation revealed this size range to be the minimum that preserved geometry upon visual inspection. Next 20 iterations of angle-weighted smoothing (AWS) were applied, which generated nearly equilateral triangles for the mesh faces. This goal is a characteristic of a well-conditioned mesh (Shewchuk, 2002). Afterward, two iterations of normal smoothing (NS) were applied. These steps in combination resulted in a reduction of surface area, as illustrated for the cell bodies of 20 cells in figure 4. Note that the surface area begins to asymptote by the second normal smoothing step, suggesting that the stair-step effect may be minimized at this point. The second round of angle-weighted smoothing and normal smoothing was performed on a subset of cells and revealed little subsequent change in somatic surface area.

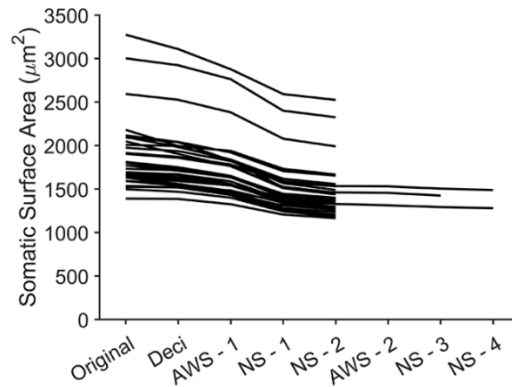


Figure 4 The change in surface area during mesh processing

We made visual inspections of the meshes during mesh processing. After the second normal smoothing, all features of the mesh are well-preserved, and the stair-step effect has been almost entirely removed (Fig. 5). Since the change in surface area was little affected by additional processing and the only change was a loss of surface features, we determined an accurate stopping point to be after the second normal smoothing.

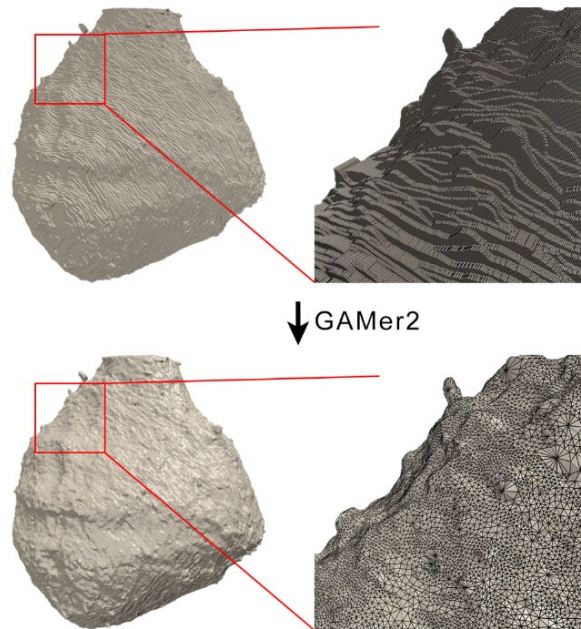


Figure 5 Mesh appearance after GAMer2 processing

3.2 Somatic Surface Areas

The somatic surface areas of GBCs span a range of 1,160 – 1,980 μm^2 and the largest GBC is visibly an outlier (Fig. 6). A Shapiro-Wilk test for normality (Shapiro and Wilk, 1965) revealed that the distribution was Gaussian without the outlier ($n = 20$; $p = 0.342$) and non-Gaussian with the outlier included ($n = 21$; $p = 0.002$). The range of somatic surface areas shows a significant difference amongst the GBC population.

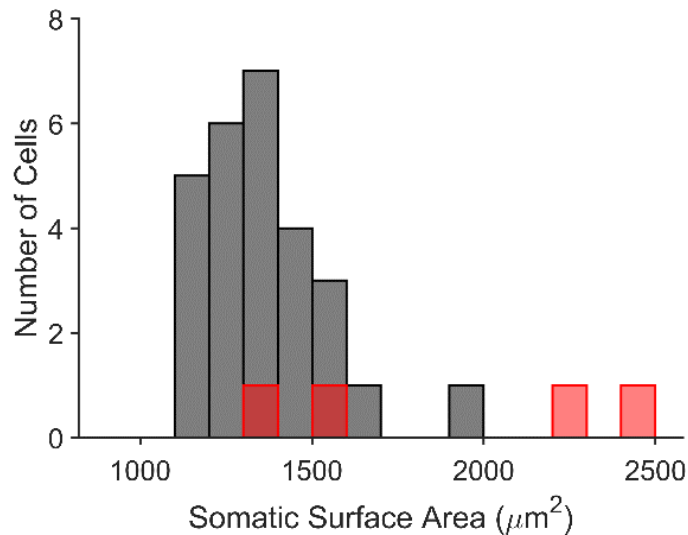


Figure 6 Somatic surface areas of AVCN neurons

3.3 Apposed Surface Areas

The endbulb nerve terminals are large, but the entire terminal is not directly apposed to the cell membrane. These areas can be filled by extended extracellular space (Cant & Morest, 1979) or by interposed glial cell processes. We generated algorithms to calculate only the area of the terminal directly apposed to the postsynaptic cell, to provide a more accurate estimate of the synaptic weight, based only on territory in which potential synapses could occur, within the computational model.

The amount of contact area (Apposed surface area or ASA) between the input terminal and the soma was determined using a custom python script (https://github.com/MCKersting12/nrrd_tools/blob/master/auto_ASA.py). This script reads the original segmented image volumes of the two objects contacting one another and resamples both image files into the same dimensional space (meaning that they have the same origin, pixel-spacing, height, width, and length). Any overlapping voxels are removed from the soma volume because the terminal segmentations were typically more accurate and there should be no voxels that were segmented as both terminal and soma. Next, the terminal is dilated by 3 voxels in the x-y plane and then another 3 voxels in all directions, this is done because the volume is anisotropic. While this difference in dilation along the three dimensions does serve to compensate for the anisotropic voxels it does not dilate the same physical length in all dimensions. We decided not to dilate by the same physical length in all directions because there was a higher degree of error in the z-dimension. Considering this we visualized some of the results of the ASA script using a variety of different dilations and decided that the 3 voxels in x and y and then 3 voxels in x, y, and z lead to a good result. The overlapping region between the dilated terminal and the soma volume is extracted as a separate volume, and the marching cubes algorithm is performed on this separated volume. The surface area of the resultant mesh, which appears as a flattened volume, is divided by two because we are only interested in the contact area to generate the ASA.

Figure 7 shows the size of all somatic input terminals reconstructed in the EM volume. There is a large peak in the histogram in the range of the very smallest terminals. The GBC cell body is covered by a variety of small terminals from unknown sources. Since they are very

numerous, all the small terminals were reconstructed from 1 cell, so that a representative sample of their sizes could be achieved. The number of inputs per bin decreases rapidly and exhibits a minimum at $35 \mu\text{m}^2$, which we defined as a boundary for large terminals. Since the endbulb and modified endbulb terminals originate from auditory nerve fibers (Cant & Morest, 1979; De No, 1933; Rouiller, Cronin-Schreiber, et al., 1986; Rouiller & Ryugo, 1984), as a second check on the validity of this size criterion we traced the axons of these large terminals as far as possible within the image volume. Our goal was to ascertain whether this size threshold also identified terminals most likely to be traced to a myelinated fiber within one of the auditory nerve fascicles.

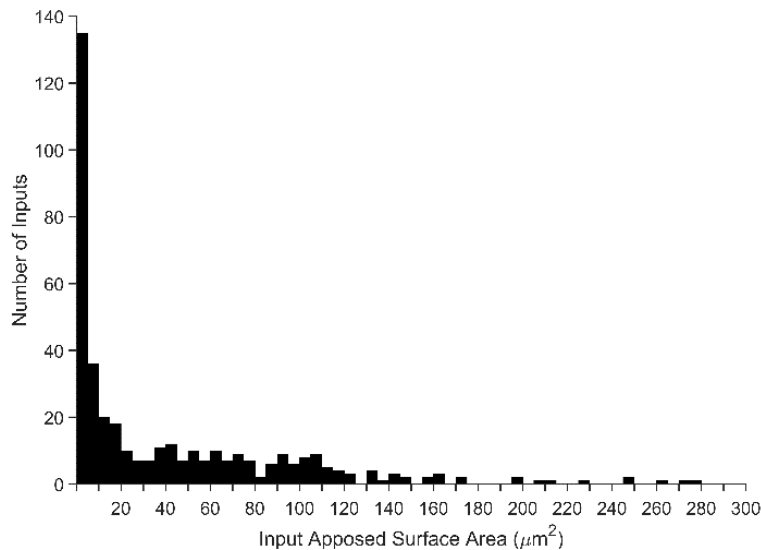


Figure 7 Input ASA for all reconstructed somatic terminals

Terminals of axon branches originating from auditory nerve fascicles are nearly entirely distributed at ASA's greater than $35 \mu\text{m}^2$, and those that are unmyelinated are predominately distributed below this threshold (Fig. 8). These data are consistent with our inference that all nerve terminals above this threshold are auditory nerve inputs and all those below this threshold

do not originate from the auditory nerve. Note that myelinated inputs cover a broad size range, so that criterion alone is not sufficient to define inputs from auditory nerve fibers.

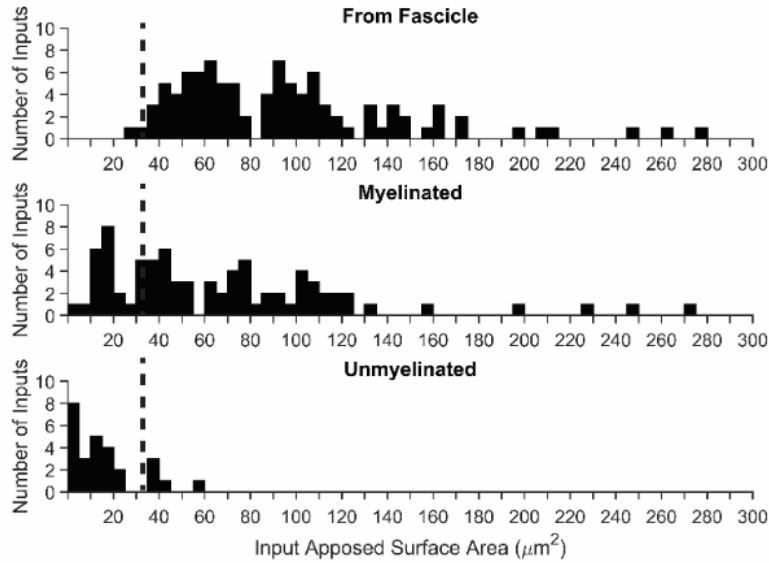


Figure 8 Terminal sizes by axon property

Cao and Oertel, 2010 found 4-6 converging auditory nerve terminals contacting GBCs in the mouse, although their methodology is prone to underestimation as discussed in the introduction. Unbiased measures from volume EM reconstructions revealed larger numbers of auditory-nerve inputs (5-12 per cell), most of which (15/21) had values greater than the maximum of six inputs that were measured in brain slices (Fig. 9).

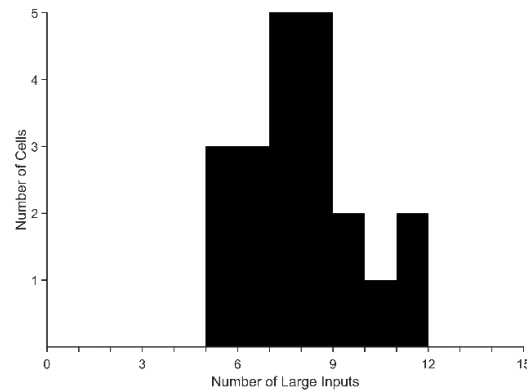


Figure 9 The number of convergent auditory nerve terminals to each GBC

The amount of somatic surface area covered by large terminals was quantified to assess variation within the GBC population. The distribution of somatic surface area coverage follows a normal distribution but spans a wide range, between 35% coverage and 65% coverage (Fig. 10).

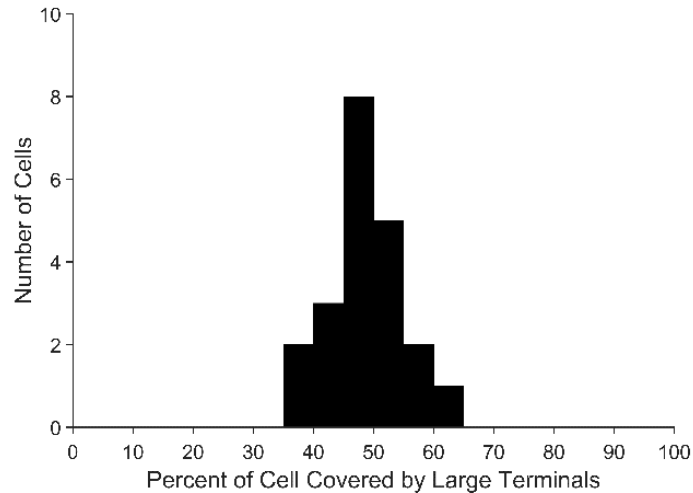


Figure 10 Somatic coverage by large terminals

The size of the auditory nerve terminals onto each GBC was also quantified. To assess different models of innervation it is important to understand the size distribution of terminals onto each GBC. For instance, a cell with 2 very large terminals will likely respond to incoming information very differently than a cell with 20 very small inputs. Figure 11 shows the input size distribution for all 21 cells reconstructed. Each line in the graph represents a cell, the inputs are in rank-order and the size of terminals is on the y-axis. After the 2nd or 3rd largest terminal the sizes of inputs across cells are tightly clustered. In contrast, the size of the largest terminal has a very large amount of variation amongst the GBC population.

When the size of the largest terminals is plotted on a histogram a break is observed between 175-200 μm^2 , separating the population nearly in half and revealing a group of cells with one or two (one cell) very large terminals. We propose that these terminals are

suprathreshold. Consequently, we suggest that some GBCs follow the coincidence detection model of innervation (Joris et al., 1994; Rothman & Young, 1996) whereas other GBCs follow a mixed model of innervation, where they have one or two suprathreshold inputs along with a set of smaller, subthreshold inputs.

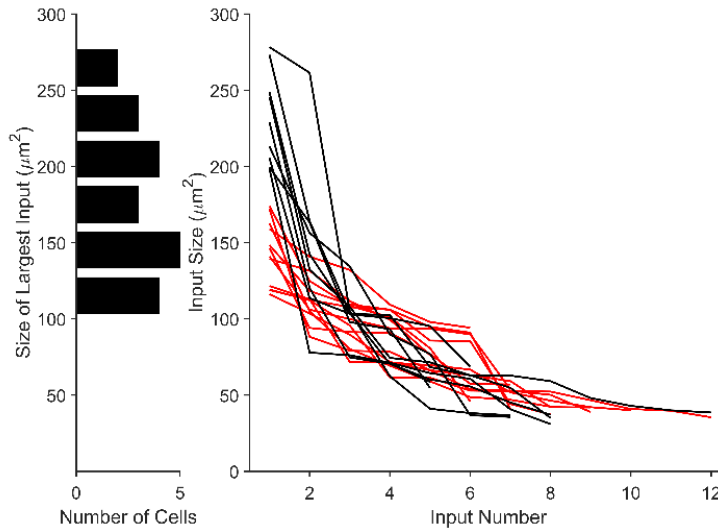


Figure 11 Terminal size distribution

3.4 Terminal – Fascicle Relationships

Multiple type 1 spiral ganglion cells are innervated by a single inner hair cell (Liberman & Oliver, 1984), so it stands to reason that AN fibers near one-another share some correlation in their activity. Groups of axons can be visualized moving through the EM volume in a tightly packed manner, so the rates of convergence of different groups of axons (from here on out referred to as fascicles) to a single GBC were assessed. In figure 12 multiple AN fibers are seen converging to single GBCs. In panel A there are two AN fibers (green and purple) that are right next to one another in the fascicle, whereas in panel B all AN fibers come from different groups of fascicles. This suggests that there may be some relationship between inner-hair cell channel and GBC innervation.

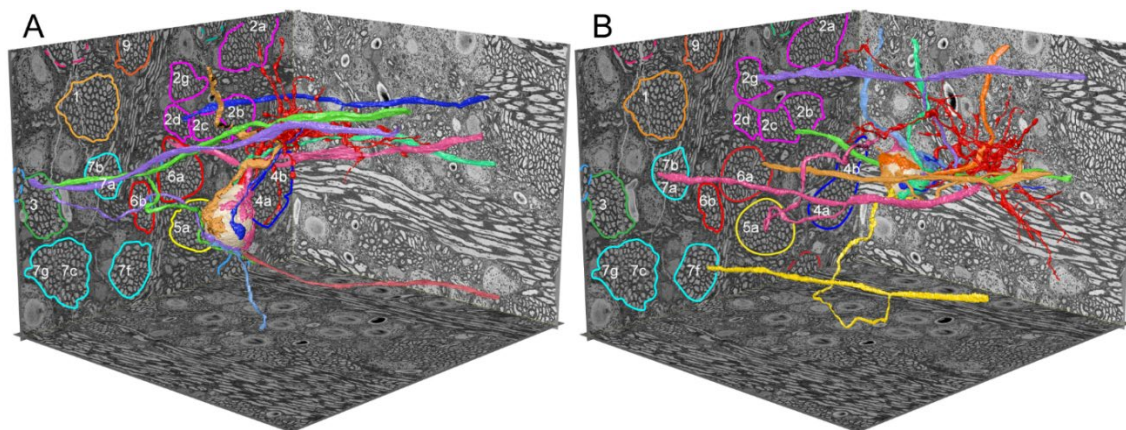


Figure 12 Convergence of auditory nerve fascicles to GBCs

After the fascicles were labeled in detail, we decided to assess whether all groups innervate GBCs in the EM volume equally. To assess this each terminal had its axon tracked back to its origin and the number of axons per fascicle was counted. There are a couple of axon fascicles that preferentially have nerve terminal branches that contact GBCs in the EM volume (fig. 13). This suggests that certain inner-hair cell channels innervate certain regions of the AVCN with a higher density.

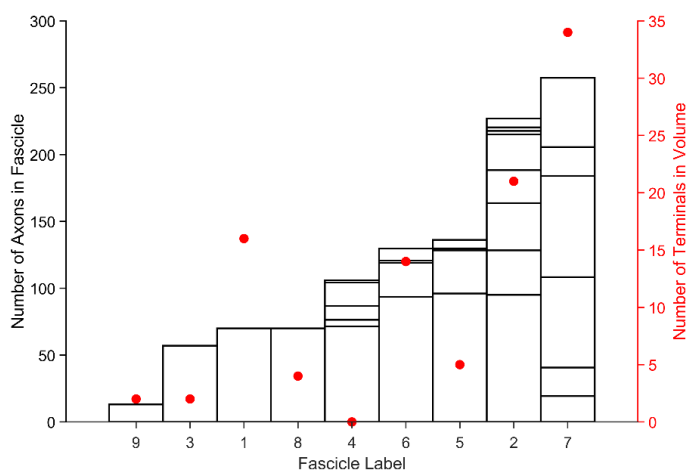


Figure 13 Terminal contribution by fascicle label

The axonal convergence was also assessed on a cell-to-cell basis. The results can be seen in figure 14. Each GBC receives a different complement of nerve terminals based on their origin

and myelination patterns. Due to the constraints of the EM volume, those cells that are large and not from a defined fascicle are still inferred as stemming from the auditory nerve. The inset-histogram shows that there is a wide range of convergence amongst GBCs.

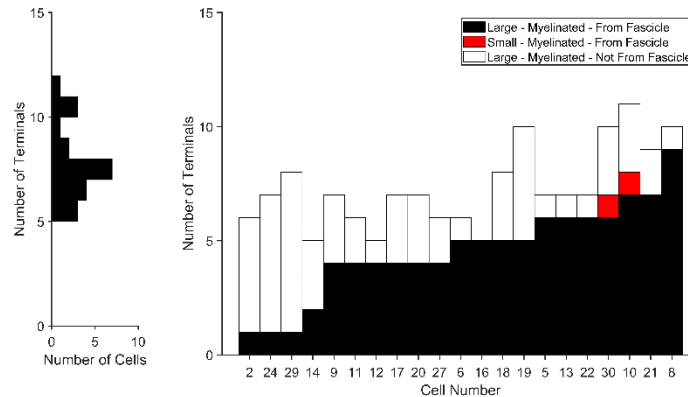


Figure 14 Converging terminals separated by axon property and contacted cell

3.5 Models of Input Convergence

The two models of innervation were assessed in a computational framework to analyze their validity. Figure 15 shows all large terminals contacting two GBCs, the left has only similarly-sized terminals and the right GBC has several similarly sized terminals and a single-large terminal covering almost $250 \mu\text{m}^2$. The modeling was performed by a collaborator – Paul Manis, Ph.D. using the model outlined in Campagnola and Manis, 2018. The traces show voltage recording from a GBC over several trials. During these simulations only a single input was active, the input number corresponds to the rank-order of the terminals onto that cell. The traces on the left show 10 inputs that are all incapable of driving an action potential alone. The traces on the right show 7 subthreshold inputs and a single suprathreshold input that can drive the GBC to spike. These results confirm that GBCs are following two models of innervation. The GBC on the left is following the coincidence detection model and the GBC on the right is following the mixed model.

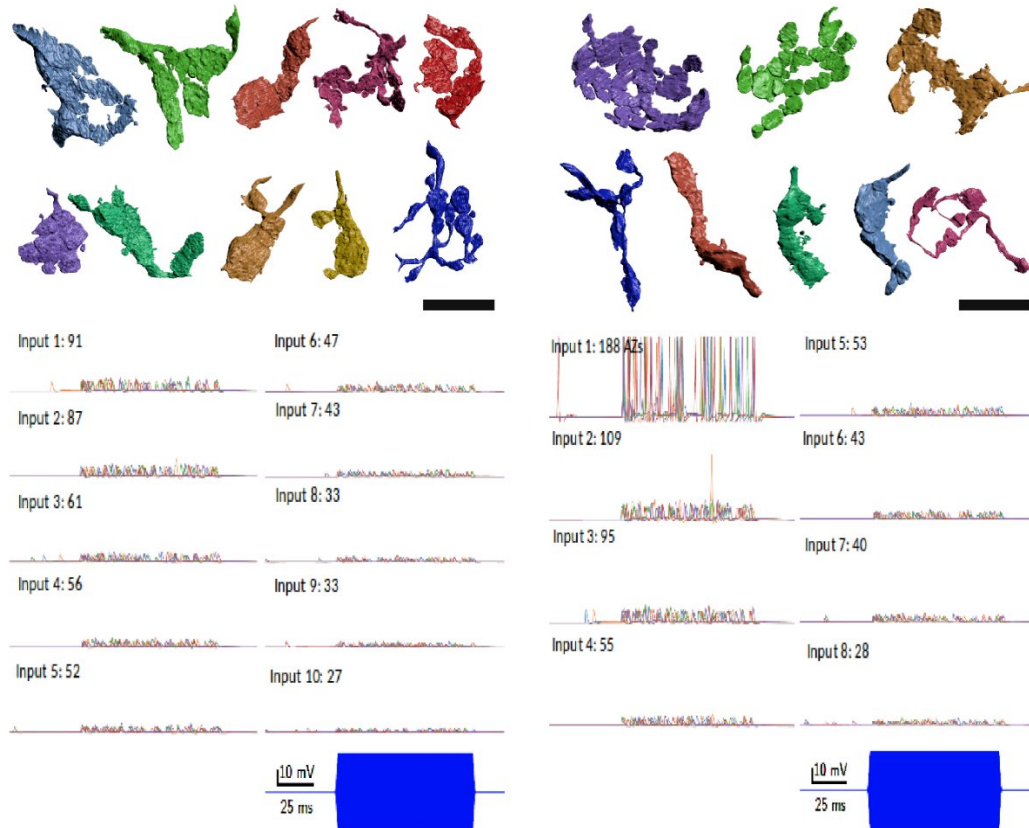


Figure 15 Two models of innervation assessed in a computational framework

3.6 Synapse Distribution

One of the goals of this thesis is to provide all quantitative metrics necessary to build accurate compartmental models of GBCs. One crucial part of modeling is setting the synaptic weight of the nerve terminals. The synaptic weight is essentially the average excitatory post-synaptic conductance caused by the activation of a given nerve terminal. To assess the strength of the nerve terminals we found the average number of synapses relative to the apposed surface area ($0.7686 \text{ synapses} / \mu\text{m}^2$). This was done by averaging the synaptic densities of 23 separate nerve terminals of varying sizes (Figure 16). While counting the synaptic densities no significant differences were found amongst the population (based on a negative result on the Shapiro-Wilk

test for normality). For each terminal in the model, the size of ASA is multiplied by this synaptic density to reach an estimation of the number of synapses in each nerve terminal.

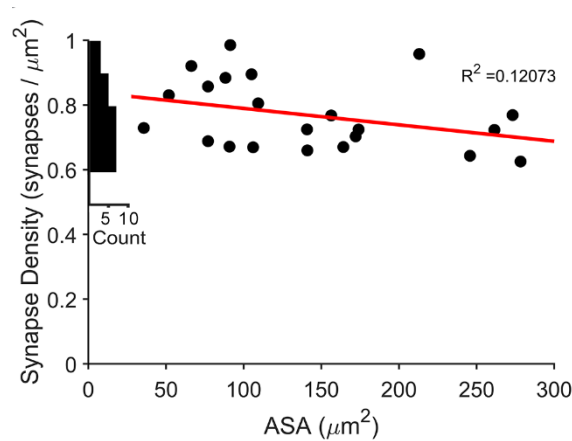
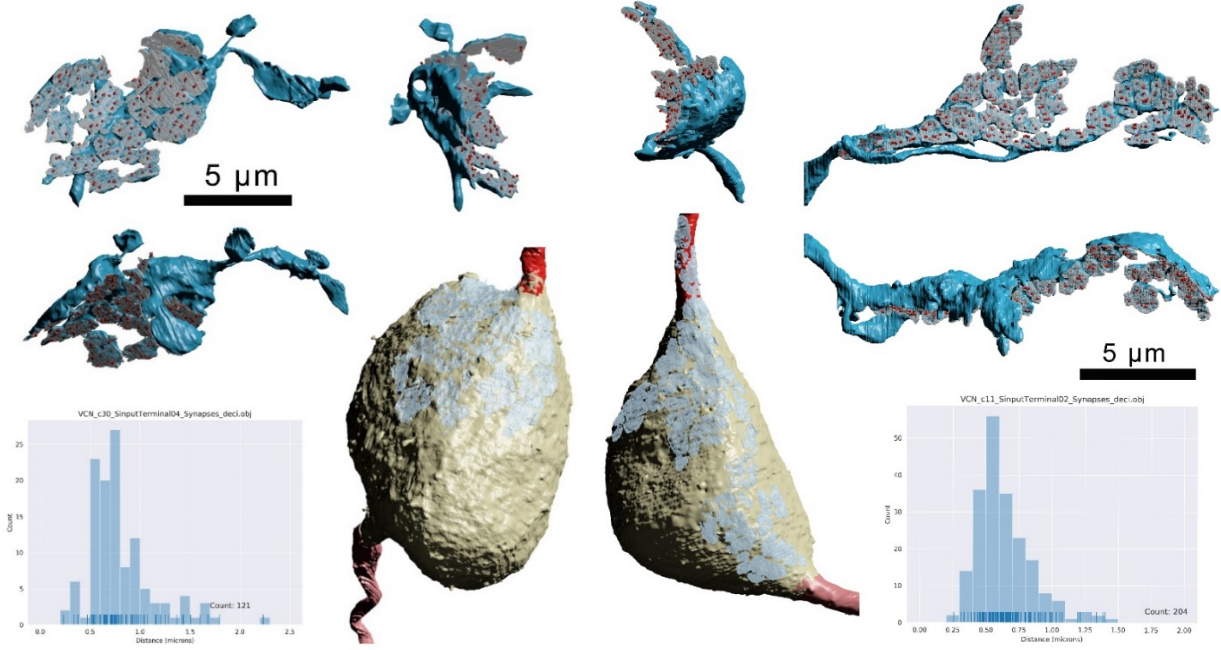


Figure 16 Synapse counts relative to ASA

During synapse quantification, it was noticed that the synapses are uniformly distributed in the terminal. To assess this in a quantitative manner custom software was written – it is publicly available at https://github.com/MCKersting12/Distribution_Analysis. Briefly, it reads in a mesh file that contains all synapse markings, it calculates the center point for each of the separate objects, then it calculates the distance to that synapse’s nearest neighbor. This distance is calculated for each separate synapse and all distances are plotted on a histogram. From this data, it was noticed that the synapses are regularly distributed amongst the nerve terminal. There is typically a positive skew in these distributions, suggesting there are some active zones more separated from the others. Also, while analyzing the morphology of the terminals we noticed that there are pad structures – meaning there are circular areas of contact area that branch and connect to one another (Figure 17). The morphology of these terminals will not be addressed thoroughly in this study, but it does warrant further investigation.

Soma SA = 1508.36 μm^2 ASA=172.14 μm^2

Soma SA = 1288.45 μm^2 Input ASA = 213.09 μm^2



Soma SA = 1357.62 μm^2 ASA=261.49 μm^2

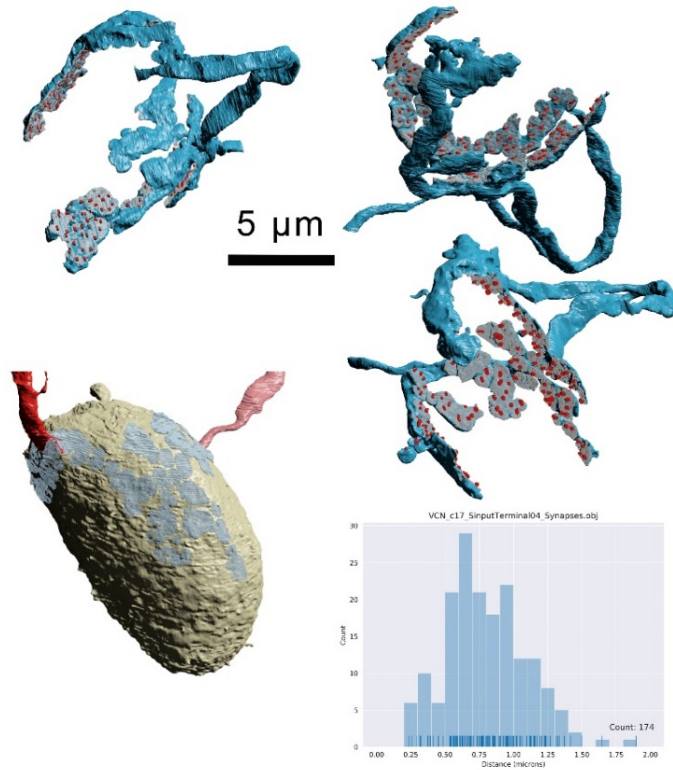


Figure 17 Distribution of synapses within the auditory nerve terminal

3.7 Dendrite Structure

The bushy cell dendrite extends for a short distance away from the soma before branching in all different directions, this gives the dendrite a tufted – “bushy” – appearance. A rendition of one of the cells with its inputs is shown in Figure 18. The dendritic tree of the bushy cell is very complex given the short distance that it spans. Due to the high-resolution nature of the reconstructions, separate dendritic elements can be thoroughly analyzed. We noted 4 main components of the dendrite: the proximal dendrite, dendritic hubs, dendritic tubes (distal dendrite), and dendritic swellings. The rigorous separation of these components is only achievable through high-resolution imaging.

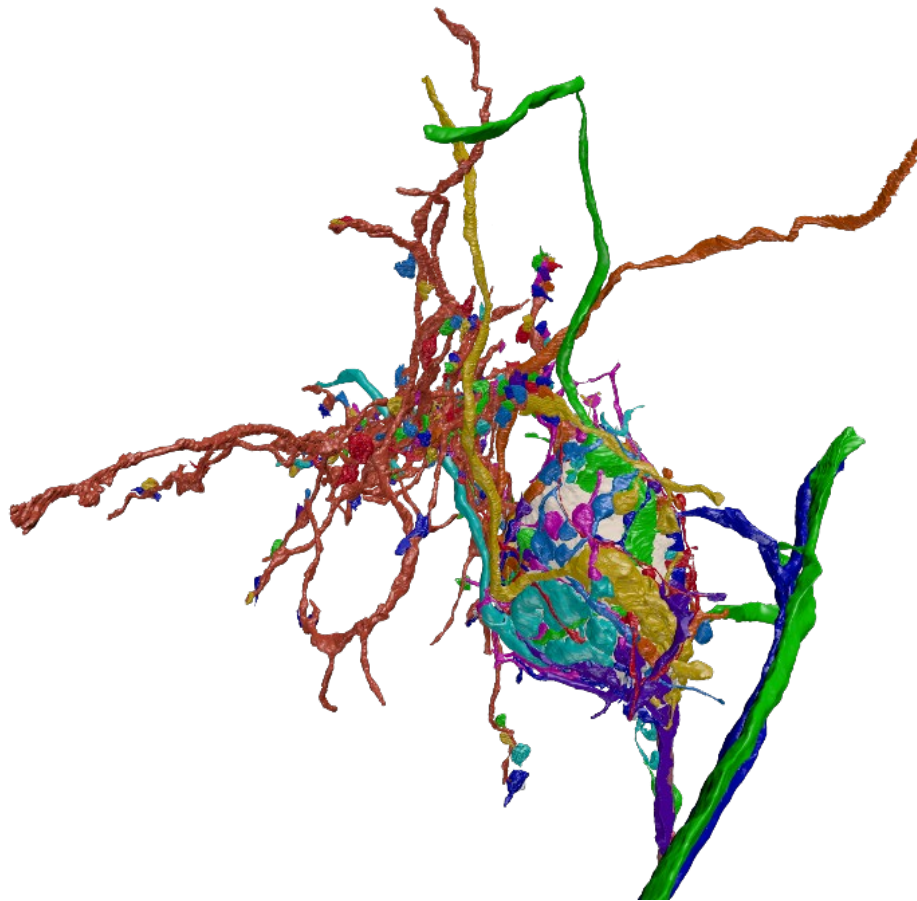


Figure 18 A bushy cell with its dendritic tree and all terminals

The proximal dendrite extends from the cell body about 2 to 5 microns and rarely has branches, if there are branches then they are generally short and sparse. Dendritic hubs are defined as a section of the dendrite, spanning a short distance, that has a 1.5X radius increase on the proximal and distal end, and has more than a single branch point. Dendritic swellings are defined as a section of the dendrite, spanning a short distance, that has a 1.5X radius increase on the proximal and distal end, but has 1 or no branch points. Tubular dendrite is defined as the remaining dendrite.

The structure of the bushy cell dendrite typically follows a pattern: there is a proximal dendrite that spans 2-5 microns from the somatic surface, this is followed by a dendritic hub (sometimes referred to as the main hub) which begins the profuse branching pattern. All branches from the main hub contain tubular dendrite interspersed with swellings and occasionally an additional hub.

Dendritic swellings occur very frequently throughout the dendritic tree (fig. 19). The branching patterns and morphological analysis were performed on the swc version of the dendrites, so a python tool-kit was developed to process/analyze these files: <https://github.com/MCKersting12/pyswc>. One aspect of this toolkit allows for easy quantification of the counts of disconnected components and their surface areas. Implementing this software, we found that each dendrite in the EM volume has between 60 and 140 separate dendritic swellings, and the swellings (fig. 20), on average, consist of over one-quarter of the surface area of the dendrite (fig. 21).

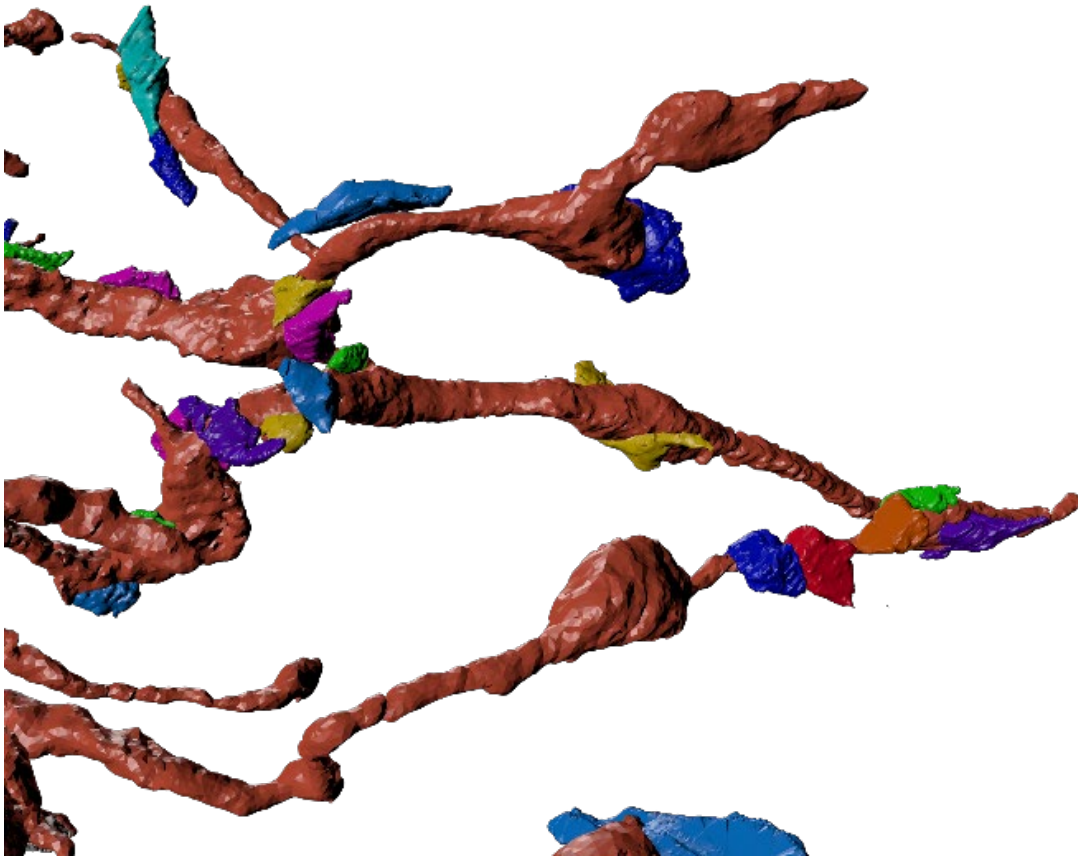


Figure 19 Swellings and shafts on a GBC dendrite

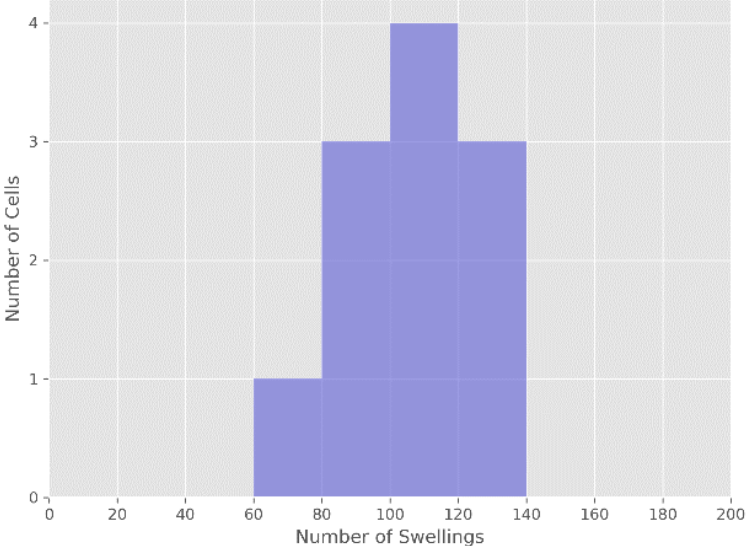


Figure 20 Distribution of swelling counts per dendrite

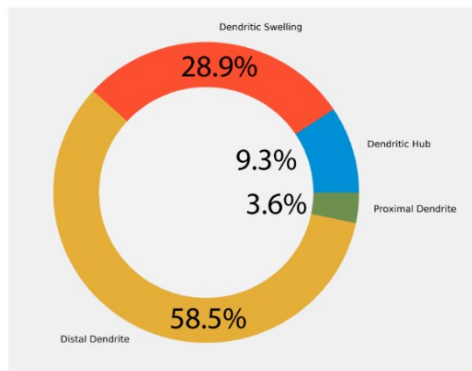


Figure 21 Composition of GBC dendrite surface area

Dendritic hubs occur less frequently than dendritic swellings. Each of the GBCs had between 4 and 13 distinct hubs (fig. 23). Most GBCs had a main hub (fig. 22), which is larger and has more branch points, at the distal end of the proximal dendrite. Those cells that had two proximal dendrites typically had two main hubs, although they were less profusely branches. A unique cytoskeletal mass (fig. 24) was seen at the center of many dendritic hubs, but its purpose is unknown.

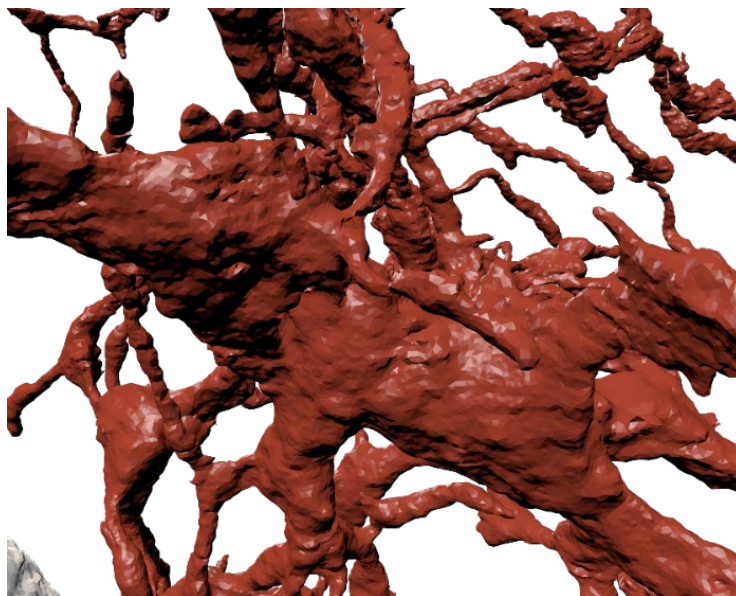


Figure 22 Close-up of the dendritic hub

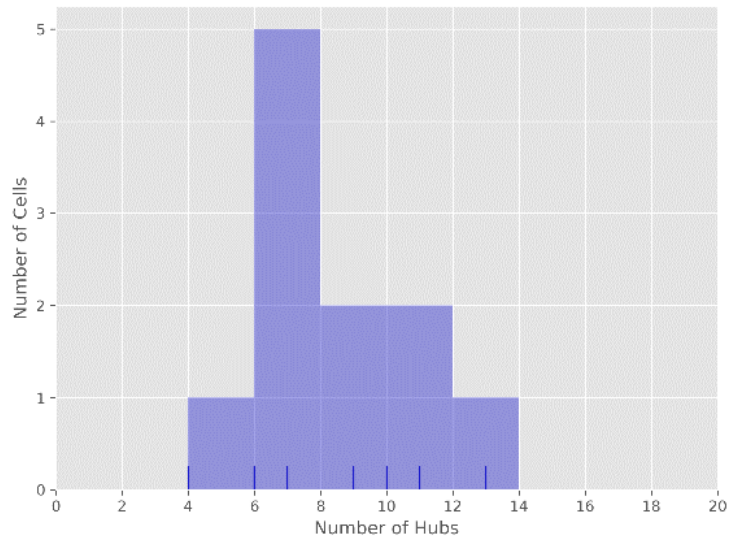


Figure 23 Distribution of hub counts per GBC

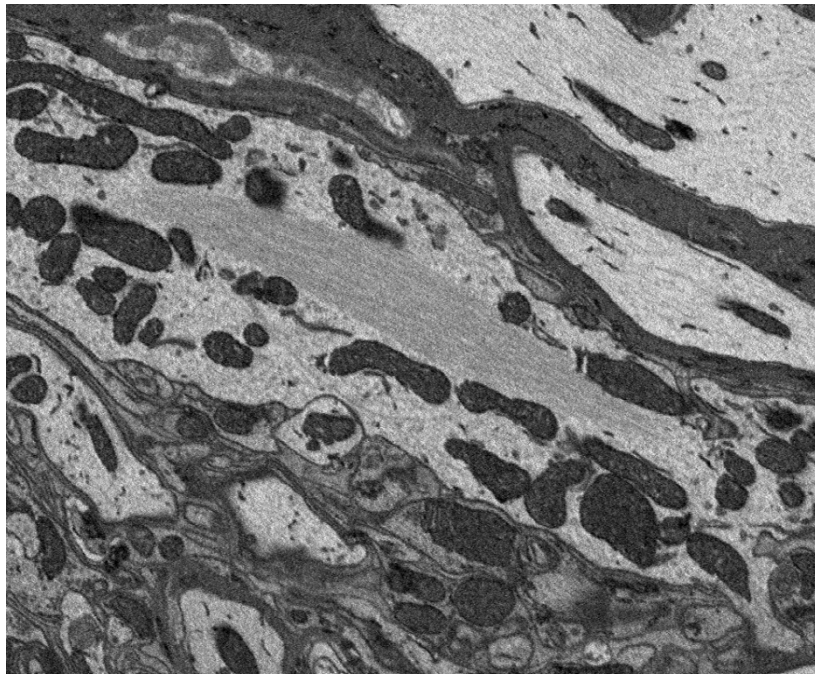


Figure 24 Unique cytoskeletal structure located in the dendritic hub

After rigorously defining these different GBC dendritic compartments we set out to see whether the patterns of innervation were different. We chose a cell with a typical dendritic tree

that was entirely contained within the EM volume and reconstructed all the nerve terminals contacting it (>200). Next, custom software was developed to find which dendrite compartment each terminal was contacting. Briefly, this script loads a terminal mesh and the dendrite swc file, it separates all disconnected components within the terminal mesh (as separate terminals connected by an axon were contained in the same mesh) and finds the center of the component. From the center of this component, it calculates the distance to each swc node, subtracts the radius of the swc node to find the distance to the swc surface, and records the node with the shortest distance. This analysis demonstrated that separate components of the dendrite are not preferentially innervated.

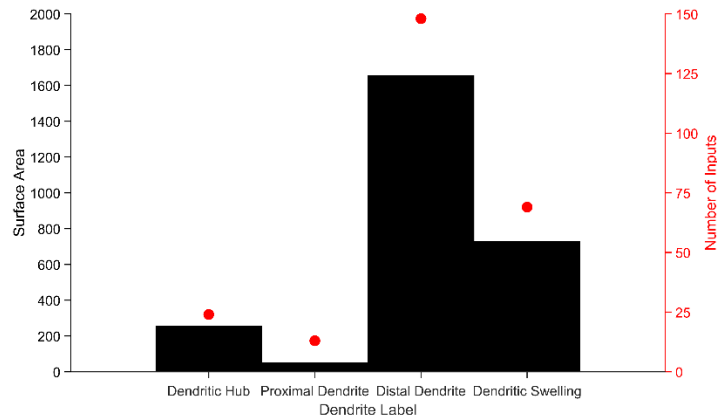


Figure 25 Distribution of terminals and surface area by dendritic component

Chapter 4: Discussion

4.1 Precise Meshing Algorithms Allow for More Biologically Realistic Simulations

This study explored the profound impact that meshing can have on quantifying structures from electron microscopy. Depending on the stopping point defined by the user, the ending surface area can vary by 10 – 25%. This is an unacceptable amount of variation if the goal is to make accurate computational models. To counteract this problem, we implemented cutting-edge mesh processing algorithms (Lee et al., 2020). Because of this careful analysis, we present the most accurate surface area metrics to date for GBCs.

4.2 Models of Input Convergence

Five to twelve auditory nerve inputs converge onto each GBC for the 21 cells in this sample. This range is larger than estimated from electrophysiological techniques (Cao & Oertel, 2010). It is known that the electrophysiological paradigm for measuring convergent inputs is prone to underestimation. The structure of inputs also has a high degree of variance. Some terminals are calyx-like and encompass a large portion of the cell whereas some terminals are more bouton shaped.

It was originally theorized that multiple subthreshold convergent inputs would allow the bushy cell to represent temporal features of sound better than their auditory nerve afferents (Joris et al., 1994), but we propose that multiple suprathreshold inputs could also accomplish this task. Based on the size distribution of convergent terminals and the results from computational modeling we found the GBCs follow two patterns of innervation. The first model has one or two

suprathreshold inputs followed by several subthreshold inputs and the second model has only subthreshold inputs. The former is called the mixed model and the latter is called the coincidence detection model. These results can be seen in figure 15 where the EPSPs caused by individual inputs are shown, some auditory nerve terminals result in an EPSP with an amplitude of only a couple mV whereas some terminals can cause post-synaptic action potentials consistently. The functional readouts of these two innervation patterns is an interesting topic for further exploration.

4.3 Novel Observations in Electron Microcopy Volume

Such a large and high-resolution image volume offers new insights into the structure of cells and terminals in the AVCN. We discovered a new compartment, called a hub, in the dendrites of GBCs that may offer new insights into how they are processing auditory signals. GBCs have hubs and swellings in their dendrites that increase the surface area of the cell and are not differentially innervated. These structural features may be a means of increasing the capacitance of the cell and thus increasing the cell's time-constant, which has been shown as a mechanism for increasing the time-constant in auditory brainstem neurons (Srinivasan et al., 2019). Aspects of these structures that have been assessed rigorously in this study are reported earlier in this thesis. There are however a few aspects that are worth noting that have not been rigorously assessed. These may provide new insights into auditory processing in the AVCN.

Large terminals contacting GBCs are often directly apposed to one another. Because of the high-resolution image volume and the detail afforded by manual segmentation, it was observed that these large terminals can extend a process into its neighboring process. This arrangement can be seen in figure 26, where two separate terminals are colored red and green.

The top image shows two terminals where the red terminal process extends into the green terminal. This branch increases the surface area of contact by creating a solenoid-like structure. The images on the bottom show a long process from the green terminal extending into the red terminal. The purpose of these branches is not known but may be the structural correlate of some form of communication between the terminals.

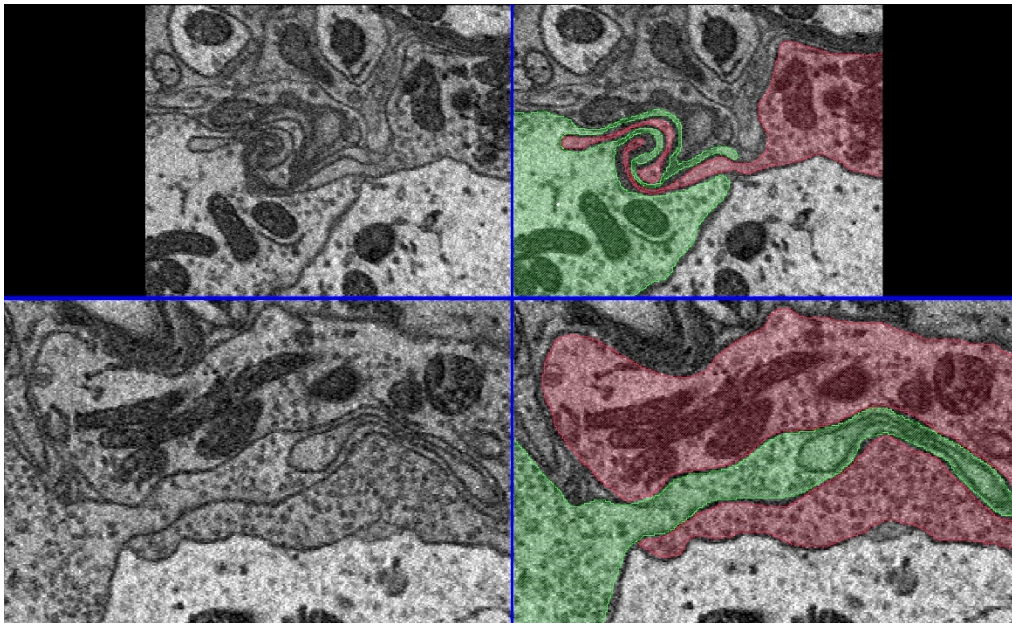


Figure 26 Large terminals have collateral branches contacting one another

There are several instances of branches from auditory nerve terminals that formed synapses on neighboring cells. This innervation pattern was most frequently observed when a bushy cell was neighbored by a large multipolar cell and suggests that a bushy cell and a neighboring large multipolar cell likely have some correlation in their activity pattern. There are also three examples of branches from the same auditory nerve input contacting multiple GBCs in the volume. Interestingly, the largest GBC is one of the two contacted cells in each of these instances. This innervation pattern supports the hypothesis that there are specializations to enhance synchronization amongst GBCs. The detection of neuron-neuron gap junctions (Ricardo

Gómez-Nieto & Rubio, 2009) is beyond the resolution of these images, but would also lead to enhanced synchrony in the output of neighboring GBCs.

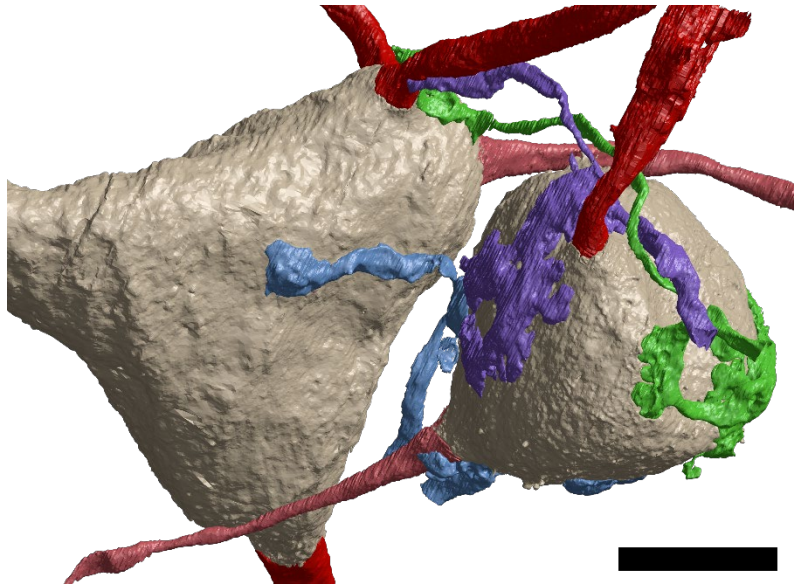


Figure 27 Large terminals have branches that contact neighboring multipolar cells

Future studies should utilize automated reconstruction methods in order to segment volume electron microscopy data more rapidly (Januszewski et al., 2018; Lee et al., 2019), as this reconstruction process requires considerable time. For a comprehensive understanding of bushy cell function, the entire VCN should be analyzed to see how the rates of convergence can vary across all of the cells in the nucleus. A full VCN reconstruction will also prove valuable to refining the modeling platform of the VCN. This effort will require large-scale data analysis, but this study lays out how those future analyses could be performed.

References

- Alibardi, L. (1998). Ultrastructural and immunocytochemical characterization of commissural neurons in the ventral cochlear nucleus of the rat. *Annals of Anatomy - Anatomischer Anzeiger*, 180(5), 427–438. [https://doi.org/10.1016/S0940-9602\(98\)80103-9](https://doi.org/10.1016/S0940-9602(98)80103-9)
- Blackburn, C. C., & Sachs, M. B. (1989). Classification of unit types in the anteroventral cochlear nucleus: PST histograms and regularity analysis. *Journal of Neurophysiology*, 62(6), 1303–1329. <https://doi.org/10.1152/jn.1989.62.6.1303>
- Bourk, T. R. (1976). *Electrical responses of neural units in the anteroventral cochlear nucleus of the cat*. Massachusetts Institute of Technology.
- Brawer, J. R., Morest, D. K., & Kane, E. C. (1974). The neuronal architecture of the cochlear nucleus of the cat. *Journal of Comparative Neurology*, 155(3), 251–299. <https://doi.org/10.1002/cne.901550302>
- Campagnola, L., & Manis, P. B. (2014). A Map of Functional Synaptic Connectivity in the Mouse Anteroventral Cochlear Nucleus. *The Journal of Neuroscience*, 34(6), 2214 LP – 2230. <https://doi.org/10.1523/JNEUROSCI.4669-13.2014>
- Cant, N B. (1981). The fine structure of two types of stellate cells in the anterior division of the anteroventral cochlear nucleus of the cat. *Neuroscience*, 6(12), 2643–2655. [https://doi.org/10.1016/0306-4522\(81\)90109-3](https://doi.org/10.1016/0306-4522(81)90109-3)
- Cant, N B, & Morest, D. K. (1979). The bushy cells in the anteroventral cochlear nucleus of the cat. A study with the electron microscope. *Neuroscience*, 4(12), 1925–1945. [https://doi.org/10.1016/0306-4522\(79\)90066-6](https://doi.org/10.1016/0306-4522(79)90066-6)
- Cant, Nell B., & Morest, D. K. (1979). The Bushy Cells in the Anteroventral Cochlear Nucleus of the Cat. A Study with the Electron Microscope.
- Cant, Nell B, & Benson, C. G. (2003). Parallel auditory pathways: projection patterns of the different neuronal populations in the dorsal and ventral cochlear nuclei. *Brain Research Bulletin*, 60(5–6), 457–474. [https://doi.org/10.1016/s0361-9230\(03\)00050-9](https://doi.org/10.1016/s0361-9230(03)00050-9)
- Cao, X.-J., & Oertel, D. (2010). Auditory nerve fibers excite targets through synapses that vary in convergence, strength, and short-term plasticity. *Journal of Neurophysiology*, 104(5), 2308–2320. <https://doi.org/10.1152/jn.00451.2010>
- Cao, X.-J., Shatadal, S., & Oertel, D. (2007). Voltage-Sensitive Conductances of Bushy Cells of the Mammalian Ventral Cochlear Nucleus. *Journal of Neurophysiology*, 97(6), 3961–3975. <https://doi.org/10.1152/jn.00052.2007>
- Carnevale, N. T., & Hines, M. L. (2006). *The NEURON book*. Cambridge University Press.
- Caspary, D. M., Backoff, P. M., Finlayson, P. G., & Palombi, P. S. (1994). Inhibitory inputs modulate discharge rate within frequency receptive fields of anteroventral cochlear nucleus neurons. *Journal of Neurophysiology*, 72(5), 2124–2133. <https://doi.org/10.1152/jn.1994.72.5.2124>

- Chanda, S., & Xu-Friedman, M. A. (2010). Neuromodulation by GABA converts a relay into a coincidence detector. *Journal of Neurophysiology*, *104*(4), 2063–2074.
<https://doi.org/10.1152/jn.00474.2010>
- Chen, C.-Y., & Cheng, K.-Y. (2005). A sharpness dependent filter for mesh smoothing. *Computer Aided Geometric Design*, *22*(5), 376–391.
<https://doi.org/https://doi.org/10.1016/j.cagd.2005.04.003>
- De No, R. L. (1933). Anatomy of the eighth nerve: III.—General plan of structure of the primary cochlear nuclei. *The Laryngoscope*, *43*(4), 327–350. <https://doi.org/10.1288/00005537-193304000-00014>
- Deerinck, T. J., Bushong, E., Thor, A., & Ellisman, M. (2010). NCMIR methods for 3D EM: A new protocol for preparation of biological specimens for serial block face scanning electron microscopy. *Nat Center Microsc Imag Res*, 6–8.
- Doucet, J R, & Ryugo, D. K. (1997). Projections from the ventral cochlear nucleus to the dorsal cochlear nucleus in rats. *The Journal of Comparative Neurology*, *385*(2), 245–264.
 Retrieved from <https://pubmed.ncbi.nlm.nih.gov/9268126>
- Doucet, John R, & Ryugo, D. K. (2006). Structural and functional classes of multipolar cells in the ventral cochlear nucleus. *The Anatomical Record Part A: Discoveries in Molecular, Cellular, and Evolutionary Biology*, *288A*(4), 331–344. <https://doi.org/10.1002/ar.a.20294>
- Englitz, B., Tolnai, S., Typlt, M., Jost, J., & RübSamen, R. (2009). Reliability of synaptic transmission at the synapses of Held in vivo under acoustic stimulation. *PloS One*, *4*(10), e7014. <https://doi.org/10.1371/journal.pone.0007014>
- Fay, R. R. (1988). Comparative psychoacoustics. *Hearing Research*, *34*(3), 295–305.
[https://doi.org/https://doi.org/10.1016/0378-5955\(88\)90009-3](https://doi.org/https://doi.org/10.1016/0378-5955(88)90009-3)
- Fernández, J.-J., & Li, S. (2003). An improved algorithm for anisotropic nonlinear diffusion for denoising cryo-tomograms. *Journal of Structural Biology*, *144*(1), 152–161.
<https://doi.org/https://doi.org/10.1016/j.jsb.2003.09.010>
- Ferragamo, M. J., Golding, N. L., & Oertel, D. (1998). Synaptic Inputs to Stellate Cells in the Ventral Cochlear Nucleus. *Journal of Neurophysiology*, *79*(1), 51–63.
<https://doi.org/10.1152/jn.1998.79.1.51>
- Friedland, D. R., Pongstaporn, T., Doucet, J. R., & Ryugo, D. K. (2003). Ultrastructural examination of the somatic innervation of ventrotubercular cells in the rat. *The Journal of Comparative Neurology*, *459*(1), 77–89. <https://doi.org/10.1002/cne.10603>
- Geiger, J. R., Melcher, T., Koh, D. S., Sakmann, B., Seeburg, P. H., Jonas, P., & Monyer, H. (1995). Relative abundance of subunit mRNAs determines gating and Ca²⁺ permeability of AMPA receptors in principal neurons and interneurons in rat CNS. *Neuron*, *15*(1), 193–204.
[https://doi.org/10.1016/0896-6273\(95\)90076-4](https://doi.org/10.1016/0896-6273(95)90076-4)
- Goldberg, J. M., & Brownell, W. E. (1973). Discharge characteristics of neurons in anteroventral and dorsal cochlear nuclei of cat. *Brain Research*, *64*, 35–54.
[https://doi.org/10.1016/0006-8993\(73\)90169-8](https://doi.org/10.1016/0006-8993(73)90169-8)
- Gómez-Nieto, R, Horta-Junior, J. A. C., Castellano, O., Herrero-Turrión, M. J., Rubio, M. E., & López, D. E. (2008). Neurochemistry of the afferents to the rat cochlear root nucleus: possible synaptic modulation of the acoustic startle. *Neuroscience*, *154*(1), 51–64.
<https://doi.org/10.1016/j.neuroscience.2008.01.079>

- Gómez-Nieto, Ricardo, Horta-Júnior, J. de A. C., Castellano, O., Millian-Morell, L., Rubio, M. E., & López, D. E. (2014). Origin and function of short-latency inputs to the neural substrates underlying the acoustic startle reflex. *Frontiers in Neuroscience*, *8*, 216. <https://doi.org/10.3389/fnins.2014.00216>
- Gómez-Nieto, Ricardo, & Rubio, M. E. (2009). A bushy cell network in the rat ventral cochlear nucleus. *The Journal of Comparative Neurology*, *516*(4), 241–263. <https://doi.org/10.1002/cne.22139>
- Grothe, B. (2000). The evolution of temporal processing in the medial superior olive, an auditory brainstem structure. *Progress in Neurobiology*, *61*(6), 581–610. [https://doi.org/10.1016/s0301-0082\(99\)00068-4](https://doi.org/10.1016/s0301-0082(99)00068-4)
- Hackney, C. M., Osen, K. K., Ottersen, O. P., Storm-Mathisen, J., & Manjaly, G. (1996). Immunocytochemical evidence that glutamate is a neurotransmitter in the cochlear nerve: a quantitative study in the guinea-pig anteroventral cochlear nucleus. *The European Journal of Neuroscience*, *8*(1), 79–91. <https://doi.org/10.1111/j.1460-9568.1996.tb01169.x>
- Harrison, J. M., & Warr, W. B. (1962). A study of the cochlear nuclei and ascending auditory pathways of the medulla. *Journal of Comparative Neurology*, *119*(3), 341–379. <https://doi.org/10.1002/cne.901190306>
- Haußecker, H., & Jähne, B. (1996). A tensor approach for local structure analysis in multi-dimensional images. In G. Girod, H. Niemann, & H. P. Seidel (Eds.), *3D Image Analysis and Synthesis* (pp. 171–178).
- Hormigo, S., Gómez-Nieto, R., Castellano, O., Herrero-Turrión, M. J., López, D. E., & de Anchieta de Castro E Horta-Júnior, J. (2015). The noradrenergic projection from the locus coeruleus to the cochlear root neurons in rats. *Brain Structure & Function*, *220*(3), 1477–1496. <https://doi.org/10.1007/s00429-014-0739-3>
- Horta-Júnior, J. de A. C., López, D. E., Alvarez-Morujó, A. J., & Bittencourt, J. C. (2008). Direct and indirect connections between cochlear root neurons and facial motor neurons: Pathways underlying the acoustic pinna reflex in the albino rat. *Journal of Comparative Neurology*, *507*(5), 1763–1779. <https://doi.org/10.1002/cne.21625>
- Jackson, H., Nemeth, E. F., & Parks, T. N. (1985). Non-N-methyl-d-aspartate receptors mediating synaptic transmission in the avian cochlear nucleus: Effects of kynurenic acid, dipicolinic acid and streptomycin. *Neuroscience*, *16*(1), 171–179. [https://doi.org/https://doi.org/10.1016/0306-4522\(85\)90054-5](https://doi.org/https://doi.org/10.1016/0306-4522(85)90054-5)
- Januszewski, M., Kornfeld, J., Li, P. H., Pope, A., Blakely, T., Lindsey, L., ... Jain, V. (2018). High-precision automated reconstruction of neurons with flood-filling networks. *Nature Methods*, *15*(8), 605–610. <https://doi.org/10.1038/s41592-018-0049-4>
- Joris, P. X., Carney, L. H., Smith, P. H., & Yin, T. C. (1994). Enhancement of neural synchronization in the anteroventral cochlear nucleus. I. Responses to tones at the characteristic frequency. *Journal of Neurophysiology*, *71*(3), 1022–1036. <https://doi.org/10.1152/jn.1994.71.3.1022>
- Josephson, E. M., & Morest, D. K. (1998). A quantitative profile of the synapses on the stellate cell body and axon in the cochlear nucleus of the chinchilla. *Journal of Neurocytology*, *27*(11), 841–864. <https://doi.org/10.1023/A:1006959532686>

- Juiz, J. M., Helfert, R. H., Bonneau, J. M., Wenthold, R. J., & Altschuler, R. A. (1996). Three classes of inhibitory amino acid terminals in the cochlear nucleus of the guinea pig. *Journal of Comparative Neurology*, 373(1), 11–26. [https://doi.org/10.1002/\(SICI\)1096-9861\(19960909\)373:1<11::AID-CNE2>3.0.CO;2-G](https://doi.org/10.1002/(SICI)1096-9861(19960909)373:1<11::AID-CNE2>3.0.CO;2-G)
- Kandler, K., & Herbert, H. (1991). Auditory projections from the cochlear nucleus to pontine and mesencephalic reticular nuclei in the rat. *Brain Research*, 562(2), 230–242. [https://doi.org/10.1016/0006-8993\(91\)90626-7](https://doi.org/10.1016/0006-8993(91)90626-7)
- Keine, C., RübSamen, R., & Englitz, B. (2017). Signal integration at spherical bushy cells enhances representation of temporal structure but limits its range. *ELife*, 6, e29639. <https://doi.org/10.7554/eLife.29639>
- Kerr, R. A., Bartol, T. M., Kaminsky, B., Dittrich, M., Chang, J.-C. J., Baden, S. B., ... Stiles, J. R. (2008). FAST MONTE CARLO SIMULATION METHODS FOR BIOLOGICAL REACTION-DIFFUSION SYSTEMS IN SOLUTION AND ON SURFACES. *SIAM Journal on Scientific Computing : A Publication of the Society for Industrial and Applied Mathematics*, 30(6), 3126. <https://doi.org/10.1137/070692017>
- Kiang, N. Y.-S. (1965). Stimulus coding in the auditory nerve and cochlear nucleus. *Acta Otolaryngologica*, 59(2–4), 186–200. <https://doi.org/10.3109/00016486509124552>
- Knutsson, H. (1989). *Representing local structure using tensors*.
- Kolston, J., Osen, K. K., Hackney, C. M., Ottersen, O. P., & Storm-Mathisen, J. (1992). An atlas of glycine- and GABA-like immunoreactivity and colocalization in the cochlear nuclear complex of the guinea pig. *Anatomy and Embryology*, 186(5), 443–465. <https://doi.org/10.1007/BF00185459>
- Lauer, A. M., Connelly, C. J., Graham, H., & Ryugo, D. K. (2013). Morphological characterization of bushy cells and their inputs in the laboratory mouse (*Mus musculus*) anteroventral cochlear nucleus. *PLoS One*, 8(8), e73308–e73308. <https://doi.org/10.1371/journal.pone.0073308>
- Lee, C., Laughlin, J., Angliviel de La Beaumelle, Amaro, R., McCammon, JA Ramamoorthi, R., Holst, M. J., & Rangamani, P. (2020). 3D mesh processing using GAMer 2 to enable reaction-diffusion simulations in realistic cellular geometries. *PLoS Computational Biology*, 16(4). <https://doi.org/https://doi.org/10.1371/journal.pcbi.1007756>
- Lee, K., Turner, N., Macrina, T., Wu, J., Lu, R., & Seung, H. S. (2019). Convolutional nets for reconstructing neural circuits from brain images acquired by serial section electron microscopy. *Current Opinion in Neurobiology*, 55, 188–198. <https://doi.org/https://doi.org/10.1016/j.conb.2019.04.001>
- Lieberman, M. C. (1991). Central projections of auditory-nerve fibers of differing spontaneous rate. I. Anteroventral cochlear nucleus. *The Journal of Comparative Neurology*, 313(2), 240–258. <https://doi.org/10.1002/cne.903130205>
- Lieberman, M. C., & Oliver, M. E. (1984). Morphometry of intracellularly labeled neurons of the auditory nerve: correlations with functional properties. *The Journal of Comparative Neurology*, 223(2), 163–176. <https://doi.org/10.1002/cne.902230203>
- López, D. E., Saldaña, E., Nodal, F. R., Merchán, M. A., & Warr, W. B. (1999). Projections of cochlear root neurons, sentinels of the rat auditory pathway. *Journal of Comparative Neurology*, 415(2), 160–174. [https://doi.org/10.1002/\(SICI\)1096-9861\(19991213\)415:2<160::AID-CNE2>3.0.CO;2-C](https://doi.org/10.1002/(SICI)1096-9861(19991213)415:2<160::AID-CNE2>3.0.CO;2-C)

- Lorensen, W. E., & Cline, H. E. (1987). Marching Cubes: A High Resolution 3D Surface Construction Algorithm. *SIGGRAPH Comput. Graph.*, *21*(4), 163–169. <https://doi.org/10.1145/37402.37422>
- Low, K., & Tan, T. (1997). Model simplification using vertex-clustering. In *3D '97*.
- Manis, P B, & Marx, S. O. (1991). Outward currents in isolated ventral cochlear nucleus neurons. *Journal of Neuroscience*, *11*(9), 2865–2880. <https://doi.org/10.1523/JNEUROSCI.11-09-02865.1991>
- Manis, Paul B, & Campagnola, L. (2018). A biophysical modelling platform of the cochlear nucleus and other auditory circuits: From channels to networks. *Hearing Research*, *360*, 76–91. <https://doi.org/https://doi.org/10.1016/j.heares.2017.12.017>
- Manis, Paul B, Xie, R., Wang, Y., Marrs, G. S., & Spirou, G. A. (2012). The Endbulbs of Held BT - Synaptic Mechanisms in the Auditory System. In L. O. Trussell, A. N. Popper, & R. R. Fay (Eds.) (pp. 61–93). New York, NY: Springer New York. https://doi.org/10.1007/978-1-4419-9517-9_4
- Martin, M. R. (1985). Evidence for an excitatory amino acid as the transmitter of the auditory nerve in the in vitro mouse cochlear nucleus. *Hearing Research*, *20*(3), 215–220. [https://doi.org/10.1016/0378-5955\(85\)90026-7](https://doi.org/10.1016/0378-5955(85)90026-7)
- Masterton, B., Thompson, G. C., Bechtold, J. K., & RoBards, M. J. (1975). Neuroanatomical basis of binaural phase-difference analysis for sound localization: a comparative study. *Journal of Comparative and Physiological Psychology*, *89*(5), 379–386. <https://doi.org/10.1037/h0077034>
- Merchan, M. A., Collia, F., Lopez, D. E., & Saldaña, E. (1988). Morphology of cochlear root neurons in the rat. *Journal of Neurocytology*, *17*(5), 711–725. <https://doi.org/10.1007/bf01260998>
- Ngodup, T., Goetz, J. A., McGuire, B. C., Sun, W., Lauer, A. M., & Xu-Friedman, M. A. (2015). Activity-dependent, homeostatic regulation of neurotransmitter release from auditory nerve fibers. *Proceedings of the National Academy of Sciences of the United States of America*, *112*(20), 6479–6484. <https://doi.org/10.1073/pnas.1420885112>
- Oertel, D., Wu, S. H., Garb, M. W., & Dizack, C. (1990). Morphology and physiology of cells in slice preparations of the posteroventral cochlear nucleus of mice. *The Journal of Comparative Neurology*, *295*(1), 136–154. <https://doi.org/10.1002/cne.902950112>
- Oliver, D., Cant, N., Fay, R., & Popper Editors, A. (2018). Springer Handbook of Auditory Research The Mammalian Auditory Pathways: Synaptic Organization and Microcircuits. In D. L. Oliver, N. B. Cant, R. R. Fay, & A. N. Popper (Eds.), *Springer Handbook of Auditory Research* (1st ed., Vol. 65, pp. 1–39). Springer, Cham. <https://doi.org/10.1007/978-3-319-71798-2>
- Osen, K. K. (1969). Cytoarchitecture of the cochlear nuclei in the cat. *The Journal of Comparative Neurology*, *136*(4), 453–484. <https://doi.org/10.1002/cne.901360407>
- Ostapoff, E.-M., & Morest, D. K. (1991). Synaptic organization of globular bushy cells in the ventral cochlear nucleus of the cat: A quantitative study. *Journal of Comparative Neurology*, *314*(3), 598–613. <https://doi.org/10.1002/cne.903140314>

- Perkins, G. A., Tjong, J., Brown, J. M., Poquiz, P. H., Scott, R. T., Kolson, D. R., ... Spirou, G. A. (2010). The micro-architecture of mitochondria at active zones: electron tomography reveals novel anchoring scaffolds and cristae structured for high-rate metabolism. *The Journal of Neuroscience : The Official Journal of the Society for Neuroscience*, *30*(3), 1015–1026. <https://doi.org/10.1523/JNEUROSCI.1517-09.2010>
- Peters, A., Palay, S. L., & Webster, H. D. F. (1992). The Fine Structure of the Nervous System: Neurons and Their Supporting Cells. *The Quarterly Review of Biology*, *67*(1), 80. <https://doi.org/10.1086/417517>
- Pfeiffer, R. R. (1966). Anteroventral cochlear nucleus: wave forms of extracellularly recorded spike potentials. *Science (New York, N.Y.)*, *154*(3749), 667–668. <https://doi.org/10.1126/science.154.3749.667>
- Purves, D., Fitzpatrick, D., & Mooney, R. D. (2012). The Auditory System. In *Neuroscience* (pp. 277–302). Sunderland, MA: Sinauer Associates, Inc.
- Radziwon, K. E., June, K. M., Stolzberg, D. J., Xu-Friedman, M. A., Salvi, R. J., & Dent, M. L. (2009). Behaviorally measured audiograms and gap detection thresholds in CBA/CaJ mice. *Journal of Comparative Physiology A*, *195*(10), 961–969. <https://doi.org/10.1007/s00359-009-0472-1>
- Raman, I. M., & Trussell, L. O. (1992). The kinetics of the response to glutamate and kainate in neurons of the avian cochlear nucleus. *Neuron*, *9*(1), 173–186. [https://doi.org/https://doi.org/10.1016/0896-6273\(92\)90232-3](https://doi.org/https://doi.org/10.1016/0896-6273(92)90232-3)
- Rhode, W. S. (2008). Response patterns to sound associated with labeled globular/bushy cells in cat. *Neuroscience*, *154*(1), 87–98. <https://doi.org/10.1016/j.neuroscience.2008.03.013>
- Rothman, J. S., & Young, E. D. (1996, January 1). Enhancement of neural synchronization in computational models of ventral cochlear nucleus bushy cells. *Auditory Neuroscience*. Retrieved from <http://www.scopus.com/inward/record.url?scp=0029967185&partnerID=8YFLogxK>
- Rothman, J. S., Young, E. D., & Manis, P. B. (1993). Convergence of auditory nerve fibers onto bushy cells in the ventral cochlear nucleus: implications of a computational model. *Journal of Neurophysiology*, *70*(6), 2562–2583. <https://doi.org/10.1152/jn.1993.70.6.2562>
- Rouiller, E. M., Capt, M., Dolivo, M., & De Ribaupierre, F. (1986). Tensor tympani reflex pathways studied with retrograde horseradish peroxidase and transneuronal viral tracing techniques. *Neuroscience Letters*, *72*(3), 247–252. [https://doi.org/10.1016/0304-3940\(86\)90521-5](https://doi.org/10.1016/0304-3940(86)90521-5)
- Rouiller, E. M., Cronin-Schreiber, R., Fekete, D. M., & Ryugo, D. K. (1986). The central projections of intracellularly labeled auditory nerve fibers in cats: An analysis of terminal morphology. *Journal of Comparative Neurology*, *249*(2), 261–278. <https://doi.org/10.1002/cne.902490210>
- Rouiller, E. M., & Ryugo, D. K. (1984). Intracellular marking of physiologically characterized cells in the ventral cochlear nucleus of the cat. *Journal of Comparative Neurology*, *225*(2), 167–186. <https://doi.org/10.1002/cne.902250203>
- Rowland, K. C., Irby, N. K., & Spirou, G. A. (2000). Specialized synapse-associated structures within the calyx of Held. *The Journal of Neuroscience : The Official Journal of the Society for Neuroscience*, *20*(24), 9135–9144. <https://doi.org/10.1523/JNEUROSCI.20-24-09135.2000>

- Rubio, M. E., Matsui, K., Fukazawa, Y., Kamasawa, N., Harada, H., Itakura, M., ... Shigemoto, R. (2017). The number and distribution of AMPA receptor channels containing fast kinetic GluA3 and GluA4 subunits at auditory nerve synapses depend on the target cells. *Brain Structure and Function*, 222(8), 3375–3393. <https://doi.org/10.1007/s00429-017-1408-0>
- Ryugo, D. K., & Sento, S. (1991). Synaptic connections of the auditory nerve in cats: relationship between endbulbs of held and spherical bushy cells. *The Journal of Comparative Neurology*, 305(1), 35–48. <https://doi.org/10.1002/cne.903050105>
- Shewchuk, J. (2002). What Is a Good Linear Finite Element? - Interpolation, Conditioning, Anisotropy, and Quality Measures. *Proceedings of the 11th International Meshing Roundtable*, 73.
- Smith, P. H., & Rhode, W. S. (1987). Characterization of HRP-labeled globular bushy cells in the cat anteroventral cochlear nucleus. *The Journal of Comparative Neurology*, 266(3), 360–375. <https://doi.org/10.1002/cne.902660305>
- Spirou, G., Rager, J., & Manis, P. (2005). Convergence of auditory-nerve fiber projections onto globular bushy cells. *Neuroscience*, 136, 843–863. <https://doi.org/10.1016/j.neuroscience.2005.08.068>
- Spirou, G A, Brownell, W. E., & Zidanic, M. (1990). Recordings from cat trapezoid body and HRP labeling of globular bushy cell axons. *Journal of Neurophysiology*, 63(5), 1169–1190. <https://doi.org/10.1152/jn.1990.63.5.1169>
- Spirou, George A, Rowland, K. C., & Berrebi, A. S. (1998). Ultrastructure of neurons and large synaptic terminals in the lateral nucleus of the trapezoid body of the cat. *Journal of Comparative Neurology*, 398(2), 257–272. [https://doi.org/10.1002/\(SICI\)1096-9861\(19980824\)398:2<257::AID-CNE7>3.0.CO;2-#](https://doi.org/10.1002/(SICI)1096-9861(19980824)398:2<257::AID-CNE7>3.0.CO;2-#)
- Srinivasan, G., Dagostin, A., Leão, R. N., Balakrishnan, V., Holcomb, P., Jackson, D., ... von Gersdorff, H. (2019). Dendritic speeding of synaptic potentials in an auditory brainstem principal neuron. *BioRxiv*. <https://doi.org/10.1101/688309>
- Tolbert, L. P., Morest, D. K., & Yurgelun-Todd, D. A. (1982). The neuronal architecture of the anteroventral cochlear nucleus of the cat in the region of the cochlear nerve root: Horseradish peroxidase labelling of identified cell types. *Neuroscience*, 7(12), 3031–3052. [https://doi.org/https://doi.org/10.1016/0306-4522\(82\)90228-7](https://doi.org/https://doi.org/10.1016/0306-4522(82)90228-7)
- Trune, D. R., & Morgan, C. R. (1988). Influence of developmental auditory deprivation on neuronal ultrastructure in the mouse anteroventral cochlear nucleus. *Brain Research*, 470(2), 304–308. [https://doi.org/10.1016/0165-3806\(88\)90249-0](https://doi.org/10.1016/0165-3806(88)90249-0)
- Trussell, L. O., & Oertel, D. (2018). Microcircuits of the Dorsal Cochlear Nucleus. In Douglas L. Oliver, Nell B. Cant, Richard R. Fay, Arthur N. Popper (Ed.), *The Mammalian Auditory Pathways: Synaptic Organization and Microcircuits*. Springer, Cham. <https://doi.org/https://doi.org/10.1007/978-3-319-71798-2>
- Typlt, M., Haustein, M. D., Dietz, B., Steinert, J. R., Witte, M., Englitz, B., ... Rübsamen, R. (2010). Presynaptic and postsynaptic origin of multicomponent extracellular waveforms at the endbulb of Held-spherical bushy cell synapse. *The European Journal of Neuroscience*, 31(9), 1574–1581. <https://doi.org/10.1111/j.1460-9568.2010.07188.x>
- von Gersdorff, H., & Borst, J. G. G. (2002). Short-term plasticity at the calyx of Held. *Nature Reviews. Neuroscience*, 3(1), 53–64. <https://doi.org/10.1038/nrn705>

- Wang, Y.-X., Wenthold, R. J., Ottersen, O. P., & Petralia, R. S. (1998). Endbulb Synapses in the Anteroventral Cochlear Nucleus Express a Specific Subset of AMPA-Type Glutamate Receptor Subunits. *Journal of Neuroscience*, *18*(3), 1148–1160.
<https://doi.org/10.1523/JNEUROSCI.18-03-01148.1998>
- Webster, D. B., & Trune, D. R. (1982). Cochlear nuclear complex of mice. *American Journal of Anatomy*, *163*(2), 103–130. <https://doi.org/10.1002/aja.1001630202>
- Weickert, J. (1998). *Anisotropic Diffusion in Image Processing*. (B. G. T. Stuttgart, Ed.).
- Wickesberg, R. E., & Oertel, D. (1990). Delayed, frequency-specific inhibition in the cochlear nuclei of mice: a mechanism for monaural echo suppression. *The Journal of Neuroscience : The Official Journal of the Society for Neuroscience*, *10*(6), 1762–1768.
<https://doi.org/10.1523/JNEUROSCI.10-06-01762.1990>
- Willard, F., & Ryugo, D. (1983). Anatomy of the central auditory system. In C. C. Thomas (Ed.), *The Auditory psychobiology of the mouse* (pp. 201–303). Springfield, IL: Willott JF.
- Yu, Z., & Bajaj, C. (2004). A segmentation-free approach for skeletonization of gray-scale images via anisotropic vector diffusion. *Proceedings of the IEEE Computer Society Conference on Computer Vision and Pattern Recognition*, *1*(IEEE; 2004), 415–420.
<https://doi.org/10.1109/cvpr.2004.1315062>
- Zhou, T., & Shimada, K. (2000). *An Angle-Based Approach to Two-Dimensional Mesh Smoothing*. *Proceedings of the 9th International Meshing Roundtable*.